Cornea

Physiological Effects of *Soat1* Inactivation on Homeostasis of the Mouse Ocular Surface

Amber Wilkerson,[1] Seher Yuksel,[1] Riya Acharya,[1,*] and Igor A. Butovich[1,2]

[1]Department of Ophthalmology, University of Texas Southwestern Medical Center, Dallas, Texas, United States
[2]Graduate School of Biomedical Sciences, University of Texas Southwestern Medical Center, Dallas, Texas, United States

Correspondence: Igor A. Butovich, Department of Ophthalmology, University of Texas Southwestern Medical Center, 5323 Harry Hines Blvd., Dallas, TX 75390-9057, USA; igor.butovich@utsouthwestern.edu.

*Riya Acharya was a 2023 STARS Summer Program student.

Received: May 5, 2024
Accepted: June 10, 2024
Published: July 2, 2024

Citation: Wilkerson A, Yuksel S, Acharya R, Butovich IA. Physiological effects of *Soat1* inactivation on homeostasis of the mouse ocular surface. *Invest Ophthalmol Vis Sci.* 2024;65(8):2. https://doi.org/10.1167/iovs.65.8.2

Purpose. *Soat1*/SOAT1 have been previously reported to be critical for the biosynthesis of cholesteryl esters (CEs) in the mouse Meibomian glands (MGs) as the loss of function led to an arrest of CE production and a substantial accumulation of nonesterified cholesterol in the meibum, causing an increase in its melting temperature. The purpose of this study was to further investigate the role of *Soat1* in meibogenesis and ocular surface physiology.

Methods. The mouse ocular features of knockout *Soat1*$^{-/-}$ and wild type (WT) mice were studied using various ophthalmic and histological techniques, mouse lipidomes were monitored using liquid chromatography/mass spectrometry, whereas their transcriptomes were compared to characterize the effects of the mutation on the gene expression profiles in the MG and cornea.

Results. *Soat1*$^{-/-}$ mice displayed increased tear production and severe corneal abnormalities, such as corneal thinning, (neo)vascularization, ulceration, and opacification that progressed with aging. Transcriptomic analyses led to identification of a range of significantly disrupted pathways, which included general and specific lipid metabolism-related pathways, keratinization, angiogenesis/(neo)vascularization, muscle contraction, and several other pathways. In addition, histological and histochemical experiments revealed morphological changes in the MG, cornea, and conjunctiva in *Soat1*$^{-/-}$ mice. Notably, the mRNA microarray expression level of *Soat1* in WT MGs (log2 17.5) was 1000 × of that in the mouse cornea (log2 7.5).

Conclusions. These findings suggest a direct involvement of *Soat1*/SOAT1 in MGs in maintaining ocular surface homeostasis, in general, and corneal health, specifically.

Keywords: meibomian gland (MG), cornea, lipid homeostasis, gene knockout models, meibogenesis

Meibomian gland dysfunction (MGD) and dry eye disease (DED) are widespread pathological conditions that affect the world population regardless of ethnicity, sex, and habitat. In the United States, the prevalence of MGD was estimated to be 21% of the entire population,[1] while, in Africa, it is close to 46%.[2] In the elderly (85+ years) population in Russia, the MGD prevalence was reported to be 69%,[3] while DED was diagnosed in 27% of those surveyed with a mean age of 58.5 ± 10.5 years.[4] In New Zealand, MGD was diagnosed in 61% of recruited subjects,[5] while, in Japan, symptomatic and asymptomatic MGD were found in 18% and 47% of the study subjects.[6] In India, between 15% and 32% of the population have been reported to have MGD and/or DED.[7–9]

MGD and DED are multifactorial diseases in which ocular homeostasis is disrupted leading to a variety of signs and symptoms, such as ocular desiccation, inflammation, swollen eyelids, corneal abrasions and ulceration, Meibomian gland (MG) dropout, accumulation of lipid deposits on the eyelid margins, and a range of other abnormalities. Routinely, DED is associated with either insufficient or excessive production of aqueous tears (hypo- or hypersecretory DED, respectively), obstructed MG orifices (also known as obstructive MGD), excessive production of meibum (i.e. hypersecretory, or seborrheic, MGD), and other ocular pathologies associated with MG abnormalities.

The exocrine MGs reside within the tarsal plates (TPs) of the eyelid synthesizing and excreting a unique mixture of lipids called meibum. Meibum is important for protecting the ocular surface by forming the tear film lipid layer (TFLL) which prevents tear evaporation, aids visual acuity, and lubricates the ocular surface, among other functions. Changes in the quantity and/or quality of meibum result in MGD, leading to alteration of the tear film (TF), eye irritation, and various ocular pathologies. Multiple studies, for example,[10–18] demonstrated that alterations in the lipid profiles of meibum caused by inactivating mutations in specific genes of meibogenesis[19,20] led to MGD and DED-like signs in laboratory animals.

We previously reported that the gene *Soat1* that encodes enzyme sterol O-acyltransferase-1 (SOAT1) is highly expressed in the mouse MGs and is an essential enzyme of meibogenesis, converting free (i.e. nonesterified) cholesterol (Chl) and fatty acids (FAs) into very and extremely long chain cholesterol esters (VLC/ELC CEs). The latter are vastly different from regular, much shorter, CEs found in plasma and other tissues.[11] Notably, the VLC/ELC CEs dominate the CE pool of normal meibum in humans and mice.[19] Inactivation of *Soat1* in the gene knockout (*Soat*$^{-/-}$) mice resulted in a massive shift in the balance of Meibomian lipids (MLs) with a complete loss of VLC/ELC CEs and a massive increase in Chl. Although CEs are the second most abundant lipids in meibum in humans and mice, trailing only wax esters (WEs), their specific roles in maintaining MGs and ocular surface homeostasis are yet to be evaluated. The purpose of this study was to correlate changes in the ML profiles and MG and cornea transcriptomes with associated pathological changes in the MGs and the ocular surface morphology of homozygous *Soat1*$^{-/-}$ mice.

Methods

Experimental Animals

All animal procedures used in this study were approved by the Institutional Animal Care and Use Committee of UT Southwestern Medical Center (protocol # 2016-101549, approved July 14, 2023) and were conducted in accordance with the Association for Research in Vision and Ophthalmology Guidelines. Heterozygous *Soat1*$^{+/-}$ mice were purchased from the Jackson Laboratory (B6.129S4-*Soat1*^{tm1Far}/Pgn; stock #007147; Bar Harbor, ME, USA) and bred to yield *Soat1*$^{+/+}$ (WT) and homozygous *Soat1*$^{-/-}$ knockout mice. Mice were genotyped using 3 primers described in the Jackson Laboratory protocol #24675. Common forward primer 18958 (TGC TGA CGT CTT CCT GTG TC), WT reverse primer 18959 (GAG CTG TTG GG AGT AGG TG), and mutant reverse primer oIMR6218 (CCT TCT ATC GCC TTC TTG ACG) provided the expected bands 400 bp (mutant) and 240 bp (WT). All mice were maintained on a 12-h light/dark cycle with ad libitum access to food and water. Age matched WT and mutant mice were used for all experiments. Two to 3-month-old mice were used for transcriptomic analysis of the TPs and corneas, as described before for mouse MG.[21]

Mouse Ocular Evaluation

Mice were anesthetized using ketamine/xylazine cocktail (120 mg/kg and 16 mg/kg, respectively) and mouse ocular features were assessed using a slit lamp model BQ 900 (Haag-Streit USA, Mason, OH, USA). The ocular surfaces of mice were photographed using a digital camera. Sodium fluorescein staining was used to visualize the anterior surface of the eye. Approximately 0.25 µL of 2% sodium fluorescein solution (Fluorescein-PF 2%, from Greenpark Compounding Pharmacy, Houston, TX, USA) was administered at the medial canthus, the eye was gently closed to distribute the dye, and subsequently washed with Hanks balanced salt solution with calcium chloride and magnesium chloride (HBSS; Gibco, Grand Island, NY, USA) to remove residual dye. The degree of cornea staining was measured using the cobalt blue filter and graded following the NEI/Industry workshop guidelines,[22] and the total fluorescein score for each eye was recorded. One week later, tear production was measured using Zone-Quick phenol red thread (PRT; from Ocusoft, Rosenberg, TX, USA). Mice were lightly anesthetized using ketamine/xylazine cocktail and the thread was placed in the inferior conjunctival fornix near the lateral canthus for 15 seconds using jeweler's forceps. Tear production was measured using the scale provided on the packaging of the thread.

Mouse Tissue Collection

Mice were euthanized by isoflurane followed by cervical dislocation. The TPs were excised from the eyelids using a Zeiss Stemi 508 Stereo dissecting microscope (Carl Zeiss, Oberkochen, Germany) and extraneous tissue, such as muscle and conjunctiva, were carefully removed, as described earlier.[19] The TP specimens were placed in 200 µL of RNAlater (Qiagen, Germantown, MD, USA) and stored at −20°C until the samples were taken to the Genomics and Microarray Core facility of the University of Texas Southwestern Medical Center (UTSW) for mRNA extraction and analysis. Only samples with RNA Integrity Numbers of ≥8 were analyzed. For cornea mRNA collection, the anterior chamber was punctured above the limbus using a 25g needle. To isolate the cornea, we used Vannas scissors to cut around the circumference of the globe above the limbus. The corneal button was briefly rinsed in HBSS to remove any residual iris material and/or fur, placed in 200 µL of RNAlater, and stored at −20°C. The eyes were enucleated and the extra tissue was removed and weighed to obtain eyeball weights.

Histological Evaluation of Mouse Tarsal Plates and Meibomian Glands

TPs and eyeballs were excised using the Zeiss dissecting microscope, fixed in Carson's formalin for at least 24 hours, and dehydrated in successive passages through 50%, 70%, 95%, 100% ethanol, and xylene prior to paraffin embedding. Tissue sections were cut at 4 µm using a microtome (model Shandon Finesse 325; from Thermo Shandon, Cheshire, UK) and stained with hematoxylin and eosin (H&E; StatLab, McKinney, TX, USA) or periodic acid Schiff's (PAS; StatLab, McKinney, TX, USA).

For Oil Red O (ORO; Thermo Scientific, Waltham, MA, USA) staining, fresh TPs were fixed in 4% paraformaldehyde in phosphate-buffered saline (PBS) overnight at 4°C. Samples were passed through 10%, 20%, and 30% sucrose in PBS before embedding in the Tissue-Tek optimal cutting temperature (OCT) compound (Sakura Finetek USA, Torrance, CA, USA). Then, 10 µm sections were cut using a cryostat (model Leica CM3050S; from Leica Biosystems, Deer Park, IL, USA) and stored at −20°C until staining. The 0.5% ORO stock solution was prepared by dissolving 0.5g ORO in 100 mL iso-propanol (IPA) and heated to 56°C for 1 hour. The working ORO solution was made prior to staining by diluting stock solution with de-ionized water (6:4, vol/vol), which sat for 10 minutes before filtering. Tissue slides were removed from the freezer, air-dried for 15 minutes, washed with PBS thrice for 5 minutes, and then rinsed with de-ionized water. The slides were stained with the freshly made ORO working solution for 6 minutes, washed with water twice and mounted with VectaShield with DAPI (4′,6-diamidino-2-phenylindole; Vector Laboratories, Newark, CA, USA). ORO staining was examined by fluorescent microscopy using the Texas Red stain with a 595 nm excitation filter, and DAPI with a 360 nm ultraviolet excitation filter.

Conjunctival flat mounts were prepared from the upper and lower eyelid conjunctival sheets. The lateral canthus was cut to access the conjunctiva at the upper and lower eyelids joint. The conjunctiva was held on to as scissors were used to make a cut right below the limbus and proceeding along the palpebral conjunctiva to the medial canthus as one upper lid sheet that comprised of the bulbar conjunctiva, fornix, and palpebral conjunctiva. Then, the tissue specimen was placed flat on a slide with the conjunctiva side down and left to dry at room temperature. The lower conjunctival sheet was collected in the same manner. Each mouse produced four conjunctival flat mounts. Once the conjunctival tissue dried, the tissue was peeled off leaving behind a thin layer of cells that adhered to the slide. The samples were fixed with Carson's formalin for 15 minutes, washed with water, and then stained with PAS using the manufacturer's protocol. Imaging of tissue specimens (WT, $n = 8$ and *Soat1*$^{-/-}$, $n = 10$) was conducted using a Zeiss AXIO Observer D1 microscope (Carl Zeiss, Oberkochen, Germany). To eliminate any bias, blind tests were conducted for image acquisition and goblet cell counting. Goblet cells were counted using ImageJ (Rasband, W.S., ImageJ, U. S. National Institutes of Health, Bethesda, Maryland, USA, https://imagej.net/ij/). Only goblet cells with well-defined cell bodies were counted.

Lipidomic Analyses

Lipidomic analyses of the study ML samples were conducted using previously described ultra-high-pressure isocratic liquid chromatography—high resolution mass spectrometry (LC-MS) protocols[11,23] with no modifications, unless indicated otherwise. Briefly, 2 to 4 excised mouse TPs from individual mice were extracted with 3 × 1 mL of methanol : chloroform = 1 : 2 (vol/vol) solvent mixture at 36°C. The three lipid extracts were pooled and the solvent was evaporated under a gentle stream of ultra-high pure nitrogen at 36°C. The specimens were redissolved in 1 mL of IPA and stored in sealed 2-mL autoinjector vials at −80°C until the analyses.

All LC-MS equipment – a µSample Manager-FL, a µBinary Solvent Pump, an Auxiliary Solvent Pump, a Trap Valve Manager, a Synapt G2-Si high resolution quadrupole Time-of-Flight mass spectrometer, and all LC-MS analytical software – were manufactured by Waters Corp. (Milford, MA, USA). The LC-MS experiments were carried out using a MassLynx version 4.1 software package (from Waters). The lipids were separated on a C8 BEH Acquity column (1.7 µm, 2.1 mm × 100 mm) in isocratic mode. The eluent was composed of a mixture of 95% IPA and 5% of 10 mM ammonium formate in water. To reduce the backpressure of the LC system and improve the shapes of the peaks, the LC column was thermostated at 40°C. The flow rate was maintained at 16 µL/min by the µBinary Solvent Pump. Between 0.4 µL and 1 µL of samples were injected. The analytes were detected in the atmospheric pressure chemical ionization (APCI) sensitivity mode at R ≥ 10,000 full-width-at-half-maximum (FWHM) resolution using an IonSabre II APCI ion source and a ZSpray/LockSpray housing unit (from Waters). The 0.5 µg/mL leucine-enkephalin LockSpray solution in acetonitrile : water = 1:1 (vol/vol) with 0.1% formic acid as additive was pumped by the Auxiliary Solvent Pump at a flow rate of 1.5 µL/min. The analytes were detectable in positive ion mode (PIM) almost exclusively as major $(M + H)^+$, $(M + H – H_2O)^+$, or $(M + H – FA)^+$ adducts, unless stated otherwise. Formation of sodium, potassium, and ammonium adducts of the analytes was minimal, or nonexistent. The chemical nature of the analytes was derived from their mass spectra using the EleComp and MS^E DataViewer software packages and confirmed in tandem mass spectrometry (MS/MS) fragmentation experiments.

The corneal lipids were analyzed as follows. The cornea buttons (2 from each mouse; 2 mm in diameter) were excised and extracted the same way as TPs. The dry lipid material was dissolved in 0.5 mL of IPA and stored in sealed 2-mL glass HPLC vials at −20°C until the analyses.

The cornea lipidomes were evaluated using APCI and electrospray ionization (ESI) approaches. The LC-MS-APCI experiments were conducted as described above for TP lipids. The LC-MS-ESI experiments were performed using an ESI Low-Flow ion source (from Waters). A C18 BEH Acquity column (1.7 µm, 1 mm × 100 mm) was used instead of the C8 column. The analytes were eluted with a ternary gradient of IPA, acetonitrile, and a 5% aqueous solution of ammonium formate as described before for TP lipids.[11,23]

The data were analyzed in the MassLynx (version 4.1) and Progenesis QI (version 2.3) software packages. Statistical analyses were performed in Progenesis QI, SigmaStat (version 3.5) and SigmaPlot (version 11.0) statistical analysis suites from Systat Software Inc. (San Jose, CA, USA).

Transcriptomic Analyses

Transcriptomic analyses of TPs and cornea samples were performed at the UTSW Genomics and Microarray Core facility using MTA-1 mRNA microarray chips (from Affymetrix/Applied Biosystems, purchased from Thermo Fisher Scientific, Santa Clara, CA, USA). The RNA Integrity Numbers (RINs) were between 8 and 10 for all study samples. The raw data was initially processed in the Expression Console software version 1.4 (from Affymetrix) and then exported to the Transcriptome Analysis Console version 4.02 (from the same manufacturer). The following parameters were used: Array Type: MTA-1_0; Analysis Type: Expression (Gene); Analysis Version: version 2; Positive versus Negative area under the curve (AUC) threshold: 0.7; Genome Version: mm10 (Mus musculus); Annotation: MTA-1_0.r3.na36.mm10.a1.transcript.csv; Map File: MTA-1_0_MappingFile.r1.map; Gene-Level Fold Change <-2 or >2 (unless stated otherwise); Gene-Level P value <0.05; and ANOVA Method: Ebayes.

Results

Soat1$^{-/-}$ Mouse Ocular Phenotype

Under slit lamp examination, WT mice demonstrated no changes in their ocular health and cornea clarity with aging (Figs. 1A–1C). Conversely, even young *Soat1*$^{-/-}$ mice displayed corneal pathologies, such as moderate corneal opacification, irregular corneal surface, excessive pooling of tears, and crusty eyelid margins, all of which progressed with aging (Figs. 1D–1F). Using the slit beam to evaluate the location of the corneal haze was difficult due to the hyper-reflective cornea and the slit eye phenotype of the *Soat1*$^{-/-}$ mice, but the cornea appeared thinner with hazing near the anterior stroma and epithelium. These abnormalities progressed to severe corneal opacification, neovascularization, and ulcerations that began to appear in 5-month-old mice with half of the mice developing severe cornea damage by 12 months of age (Fig. 2). In addition, the eyelids showed progressive changes with age with features such as irregular lid margin, lashes that arise from the lid margin, upturning of the lashes toward the cornea, loss of lashes, and ulcerated eyelids (see Figs. 2C, 2D). The eye lashes and lid margins had crusty lipid accumulations and thick meibum similar to those observed in human MGD associated with chronic blepharitis,[24] Meibomian seborrhea,[25] and/or seborrheic dermatitis.[26]

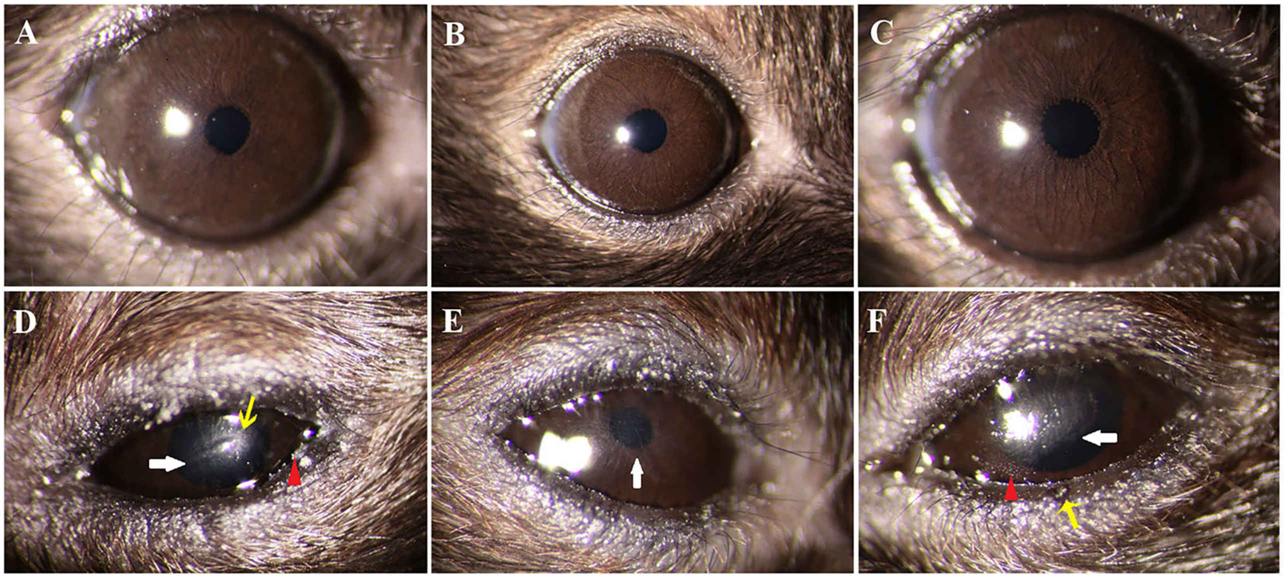

Figure 1. Ocular phenotypic abnormalities of *Soat1*$^{-/-}$ mice at 3 months, 7 months, and 12 months of age. WT slit lamp images at ages 3 months (**A**), 7 months (**B**), and 12 months (**C**) with no abnormalities to the ocular surface. (**D, E**) *Soat1*$^{-/-}$ slit lamp images of corneal abnormalities. (**D**) Three-month-old *Soat1*$^{-/-}$ mouse with an uneven corneal surface (*white arrow*), hyper-reflective cornea, and lipid accumulation around the eyelid margin (red triangle). (**E**) Seven-month-old *Soat1*$^{-/-}$ with corneal haze (*white arrow*). (**F**) Twelve-month-old *Soat1*$^{-/-}$ cornea with loss of clarity (*white arrow*), rough corneal surface, lipid particles (*red triangle*), and an irregular lid margin.

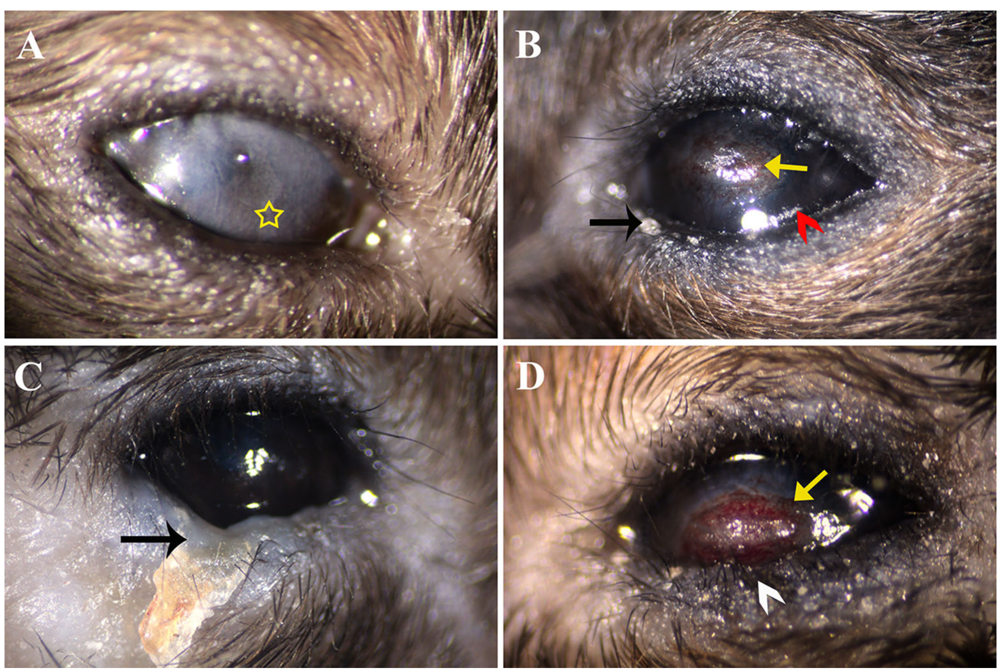

Figure 2. Progressive destruction of the cornea and eyelid of *Soat1*$^{-/-}$ mice with age. (**A**) Four-month-old *Soat1*$^{-/-}$ mouse with advanced corneal haze (*yellow star*). (**B**) Six-month-old mutant mouse with a corneal ulcer, neovascularization (*red arrow*), loss of clarity, and lipid debris (*red chevron*). (**C**) Eleven-month-old *Soat1*$^{-/-}$ with deterioration of the lower eyelid with lash loss and large crusty accumulation (*black arrow*). (**D**) *Soat1*$^{-/-}$ 12-month-old ulcerated cornea (*yellow arrow*) with changes to the lid margin and lash growth direction (*white chevron*).

Fluorescein staining of the cornea was used to identify epithelial damage, as epithelial defects are associated with increased risk of corneal ulcers, haze, and decreased vision. WT mice had minimal to no punctate staining of the corneal epithelial cells (Figs. 3A, 3B). *Soat1*$^{-/-}$ corneas revealed substantial coalescent patchy staining of the epithelium, most significant in the central cornea (Fig. 3C). In addition, there was a significant uptake of fluorescein in the conjunc-

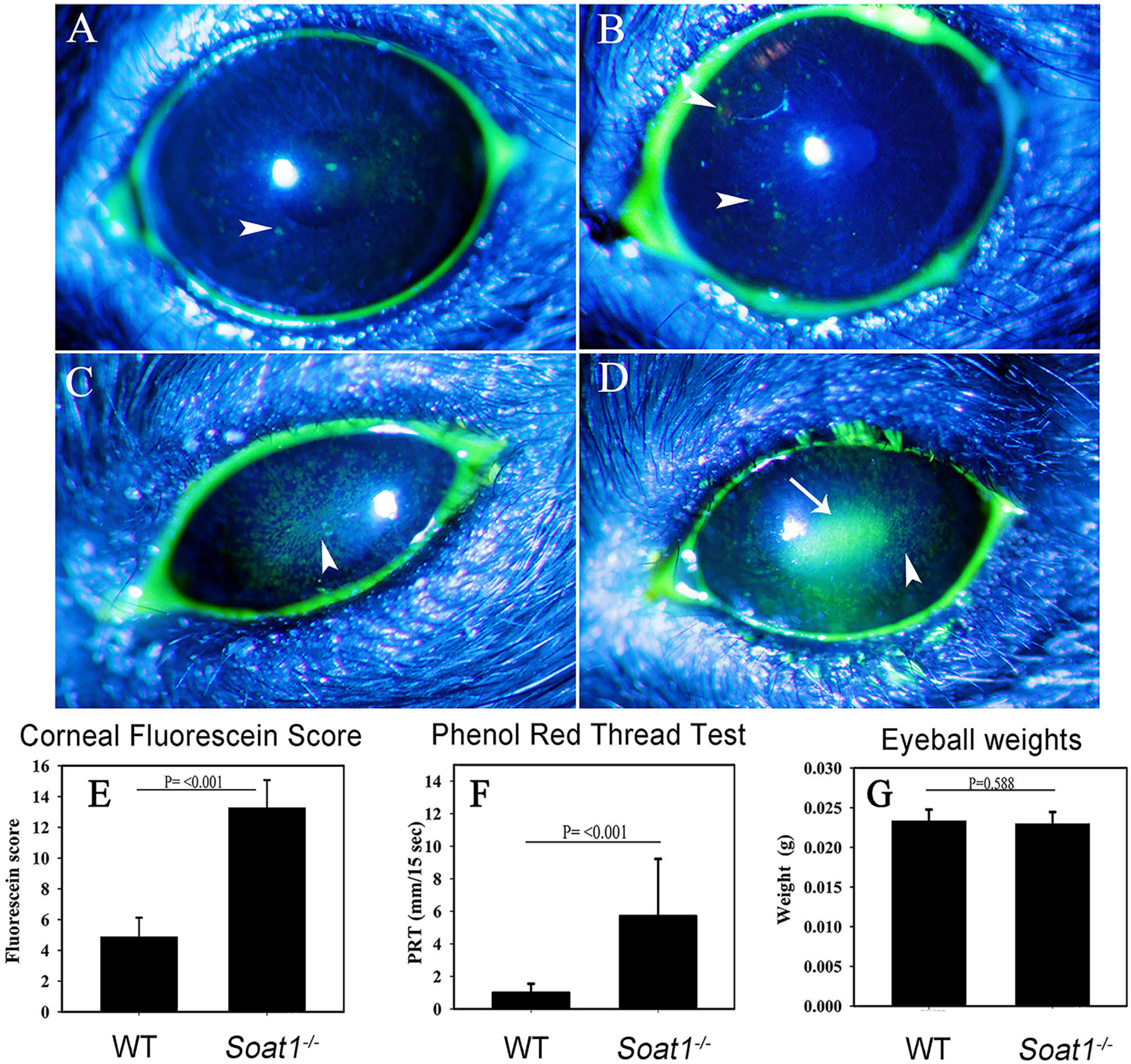

Figure 3. Fluorescein staining and ocular characteristic. (**A**) Three-month-old WT mouse with sparse epithelial staining (*white arrowhead*). (**B**) Sparse punctate staining (*white arrowhead*) of the corneal epithelium in a 12-month-old WT mouse. (**C**) Three-month-old *Soat1*$^{-/-}$ mouse with numerous coalescent staining (*white arrowhead*) of the epithelium. (**D**) Twelve-month-old *Soat1*$^{-/-}$ cornea with significant staining of the epithelium and diffusion of the dye into the stroma (*white arrowhead*). (**E**) Mutant mice ($n = 20$) had significant fluorescein staining of the cornea compared to WT controls ($n = 18$, $P = <0.001$). (**F**) Tear production of *Soat1*$^{-/-}$ mice ($n = 24$) was increased compared to WT mice ($n = 20$, $P = <0.001$). (**G**) Eyeball weights were not significantly different between *Soat1*$^{-/-}$ ($n = 10$) and WT ($n = 10$) mice ($P = 0.588$).

tiva and MG orifices (see Fig. 3C). In some instances, the *Soat1*$^{-/-}$ mice fluorescein staining diffused into the stroma and anterior chamber, indicating severe damage to the corneal epithelium or tight junctions because the stain was able to penetrate the epithelial barrier (Figs. 3D). *Soat1*$^{-/-}$ mice had a significant increase in their fluorescein scores compared to WT mice (Fig. 3E).

During the slit lamp examination, we observed excessive tear pooling around the eyelid margins of *Soat1*$^{-/-}$ mice. The tear production of *Soat1*$^{-/-}$ mice, measured using the PRT test, was increased compared to WT mice (Fig. 3F). Eyeballs of WT and *Soat1*$^{-/-}$ mice were weighed to determine if the slit eye phenotype was a result of a reduced eyeball size, but no significant differences between the two genotypes were observed (Fig. 3G).

Altered Meibomian Gland Morphology of *Soat1*$^{-/-}$ Mice

To examine whether structural or functional changes underlie the observed phenotype, TPs of WT and *Soat1*$^{-/-}$ mice were processed for histological evaluation. WT mice had the typical MG characteristics with large abundant acini

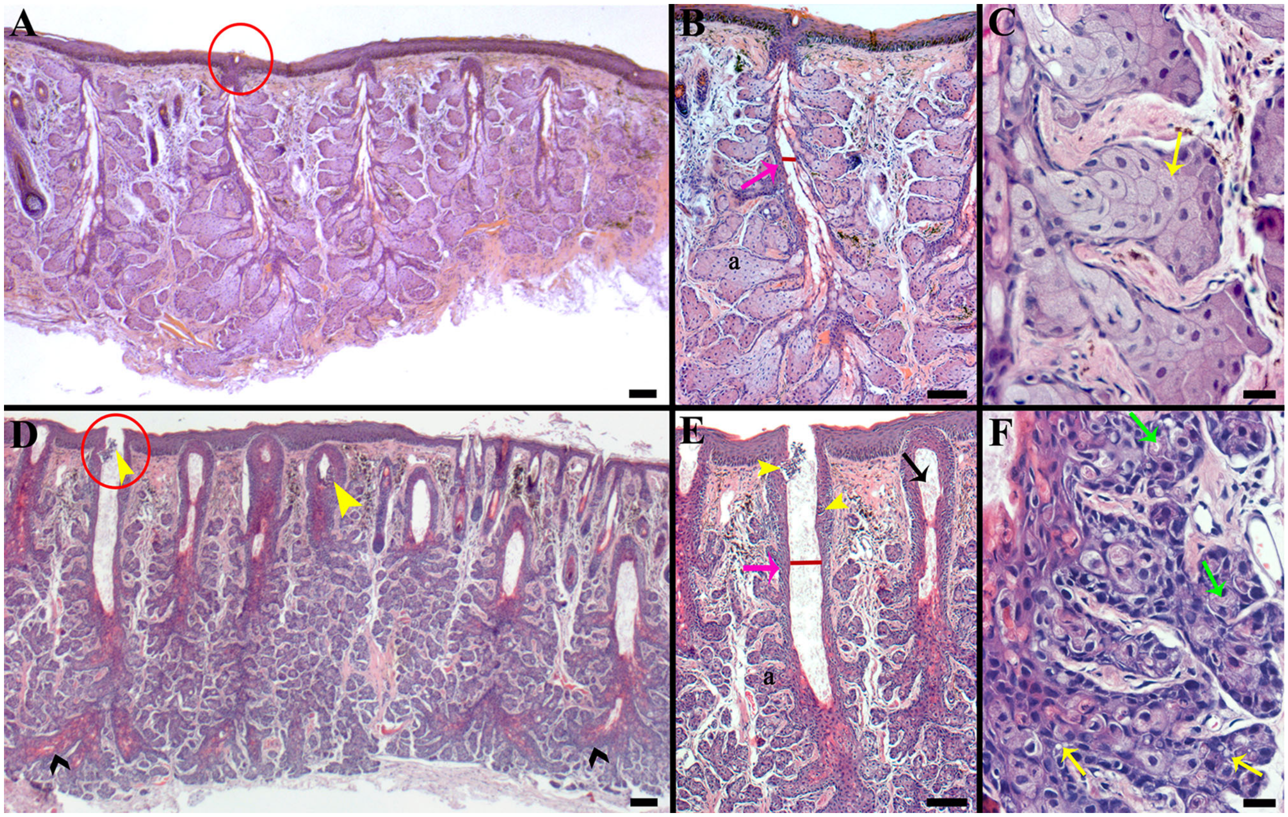

Figure 4. Morphologic alterations to the meibomian glands due to Soat1 inactivation. (**A**) WT tarsal plate at 3 months with the typical appearance of the MGs in which the plump acini (a) are connected to the central duct by connecting ducts and small orifices at the lid margin (*red circle*). (**B**) The WT MGs had a narrow central duct (*red line*) and thin ductal epithelium (*pink arrow*). (**C**) A magnified view of the WT acini shows large meibocytes with cytoplasm that are rich with lipid droplets (*yellow arrow*). (**D, E, F**) *Soat1*$^{-/-}$ 3-month-old tarsal plate with an altered morphology of the MGs. (**D**) The MG orifices were enlarged (*red circle*) with infiltration of inflammatory cells of the central duct (*yellow arrowheads*) and prominent branching of the connecting ducts (*black chevron*). (**E**) The ductal epithelium was thickened (*pink arrow*) with inflammation (*yellow arrowhead*) and enlarged central ducts (*red line*). The MGs had numerous acini (a) that were smaller and lacked the normal foamy cytoplasm of the acini. (**F**) Mutant meibocytes were small and irregular with varying sizes of lipid droplets (*yellow arrow*) throughout the acini and some meibocytes had fine needle-like spaces of the cytoplasm (*green arrow*). Hematoxylin and eosin (H&E) staining. Scale bars in panels **A**, **B**, **D**, and **E** = 100 µm; in panels **C** and **F** = 20 µm.

that secrete lipid into the central duct through narrow orifices. A magnified view of the WT acini shows large foamy meibocytes with cytoplasm rich in lipid droplets. The latter meibocytes undergo maturation and disintegration within the connecting duct leading to the central duct (Figs. 4A–4C). However, close examination of the TPs of *Soat1*$^{-/-}$ mice revealed significant changes in gland morphology caused by the mutation. *Soat1*$^{-/-}$ meibocytes were abnormally small and irregular with the loss of the uniform foamy lipid-laden cytoplasm and had variously sized lipid droplets with cytoplasmic clefts (Figs. 4D–4F). While the acini of mutant mice were smaller than those in WT mice, the *Soat1*$^{-/-}$ MGs were large and the number of acini was still high. The central duct and MG orifices of *Soat1*$^{-/-}$ mice were dilated and had inflammatory cells within the duct and ductal epithelium. In addition, the mutant ductal epithelium was thickened and hyperplastic. There was also accumulation of eosinophilic debris within the central duct. Although *Soat1*$^{-/-}$ MG acini appeared atrophic, the inspissated meibum did not result in MG dropout or shortening of the glands.

To correlate the altered meibum production with the morphological changes of the MGs, TPs of WT and *Soat1*$^{-/-}$ mice were stained with ORO. TPs of controls displayed lipid-rich MGs with a uniform distribution of lipid staining from the acini to the central duct (Fig. 5A). The lipid droplets were visible in the meibocytes of the acini until the connecting duct in which they released their contents as meibum. The lipid staining of *Soat1*$^{-/-}$ MG acini was significantly reduced with a majority of the staining occurring in the connecting ductules and the central duct. The size of *Soat1*$^{-/-}$ meibocytes varied widely, and so did lipid accumulations between neighboring cells and non-staining areas of the cytoplasm (see Fig. 5). The maturation of the *Soat1*$^{-/-}$ meibocytes also appeared to proceed differently from WT meibocytes as the former retained their cellular shape and nuclei further into the connecting ductules, as shown in Figure 5. The lipid staining of *Soat1*$^{-/-}$ meibocytes in the ductules was significantly more pronounced than the staining of WT meibocytes that underwent cellular degradation earlier in the duct.

Histopathological Changes of the Ocular Surface Due to the Inactivation of *Soat1*

Corneas of WT and *Soat1*$^{-/-}$ mice were processed for histology to investigate if morphological changes underlie

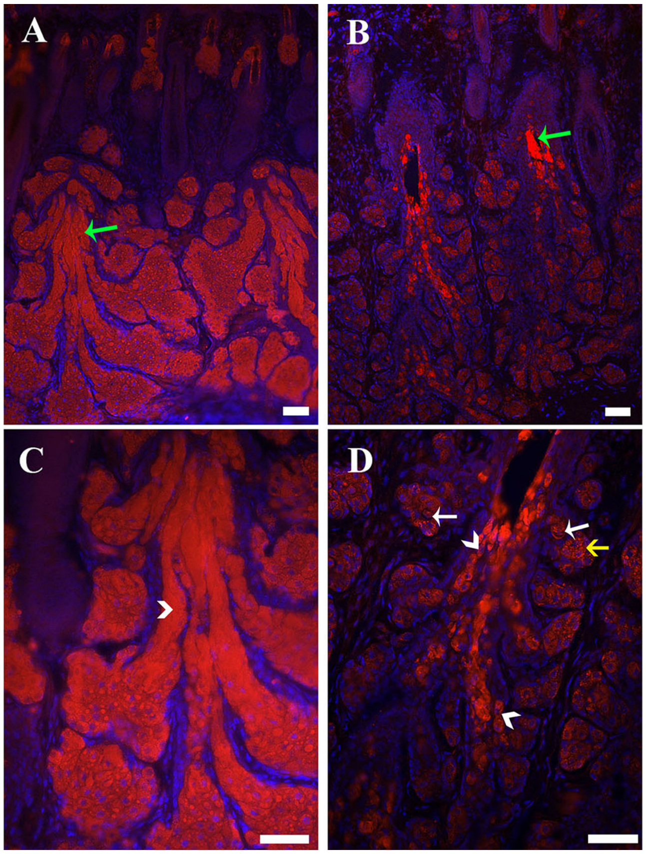

Figure 5. Oil Red O lipid staining of the Meibomian glands. (**A**) WT meibomian glands had ample ORO staining throughout the acini and ductal system (*green arrow*). (**B**) *Soat1*$^{-/-}$ meibomian glands with sparse ORO lipid staining of the acini with most lipid staining within the central duct and connecting ducts (*green arrow*). (**C**) WT meibocytes underwent disintegration within the duct (*white chevron*). (**D**) *Soat1*$^{-/-}$ meibocytes appear diverse with variations of lipid droplet accumulations (*yellow arrow*) and non-staining clefts in the cytoplasm (*white arrow*). Individual meibocytes could be seen in the connecting duct as the lipid highlighted cell shape and retained nuclei (*white chevron*). Scale bars = 50 µm.

the phenotypic changes seen in vivo with the slit lamp examination. WT mice maintained their ocular health and displayed the normal morphology of the epithelium and stroma (Figs. 6A, 6B). Low power images of corneal sections revealed the reduced corneal thickness of *Soat1*$^{-/-}$ mice compared to the WT corneas (Fig. 6C). The thickness of the stroma and epithelium varied as the epithelial/stroma interface was irregular with a jagged appearance compared to the uniform thickness of the WT corneas. The average WT central total corneal thickness was 128.15 µm and epithelial thickness was 32.82 µm, while *Soat1*$^{-/-}$ cornea was significantly thinner with the total corneal thickness of 90 µm and epithelial thickness of 19.30 µm (P <0.001). The epithelium of the *Soat1*$^{-/-}$ corneas was abnormal with flattened basal epithelial cells with necrotic cells and epithelial vacuoles. The stroma appeared condensed and hyper eosinophilic and was prone to large stromal clefts even though they were processed and stained alongside WT corneas (Fig. 6D). These corneal abnormalities progressed to severe deterioration of the cornea with epithelial vacuoles, stromal vacuoles, infiltration of inflammatory cells, hydropic change of basal cells, and focal edema in the area of epithelial loss (Figs. 6E, 6F). Evaluation of corneal ulcers showed complete loss of the central epithelium, neovascularization, fibrosis, and significant inflammation that lacked visible keratinization (Fig. 6G).

Based on the phenotypic changes seen in the cornea, we stained the tissue samples with PAS to visualize the basement membrane (BM). The BM in WT corneas was a continuous band across the peripheral and central cornea at the epithelium and stroma junction. However, *Soat1*$^{-/-}$ corneas did not have uniform staining of the BM, with frequent breaks and/or accumulations of PAS positive material in the central cornea, but maintained BM staining of the peripheral cornea (Figs. 7A, 7B). Conjunctival goblet cells were also evaluated with PAS staining. Due to the variations in goblet cell density and distribution in the conjunctiva, the middle fornix area of whole flat mounts were analyzed for a more accurate quantitation of the conjunctival goblet cells. As shown in Figures 7C and 7D, the goblet cell density increased in *Soat1*$^{-/-}$ mice compared to 3-month-old WT mice.

Comparative Analyses of Free Cholesterol and Cholesteryl Esters in Mouse Corneas

A detailed analysis of Chl and CEs of WT and *Soat1*$^{-/-}$ TP lipidomes was performed earlier.[11] For this follow-up paper, Chl and CEs of mouse corneas have been evaluated. The LC-MS experiments demonstrated that WT corneas were highly enriched in free, nonesterified Chl, whereas CEs were represented only by small amounts of C_{18-}, C_{20-}, and C_{22}–CEs, and even smaller amounts of VLC/ELC CEs. Four major cornea CEs were identified as $C_{18:1-}$, $C_{18:2-}$, $C_{20:4-}$, and $C_{22:6}$–CEs in both genotypes (Figs. 8A, 8B). The apparent Chl-to-total CE ratio in WT mice, calculated from the LC-MS abundances of their common $(Chl - H_2O + H)^+$ and $(CE - FA + H)^+$ fragment $C_{27}H_{45}{}^+$ with m/z 369.351, was 30 : 1, while the apparent molar ratio of plasma-type CEs-to-meibomian VLC/ELC CEs in the same samples varied from 6.5 : 1 to 100 : 1, or higher. For comparison, the latter molar ratio in mouse TPs was 1: 6 or lower.

Importantly, the VLC/ELC CEs (i.e. C_{22-} to C_{34}–CEs) were virtually undetectable in all *Soat1*$^{-/-}$ cornea specimens (Figs. 8C, 8D), which came as no surprise due to the complete suppression of the VLC/ELC CE biosynthesis in the MGs of *Soat1*$^{-/-}$ mice.[11] Remarkably, no differences among the profiles of 4 major corneal CEs of WT and *Soat1*$^{-/-}$ mice were observed – the same $C_{18:1-}$, $C_{18:2-}$, $C_{20:4-}$, and $C_{22:6}$–CEs were dominant species in the corneas of both genotypes, and their apparent ratios were almost identical (Fig. 9). The only CE that differed between WT and *Soat1*$^{-/-}$ mouse corneas was $C_{18:2}$–CE, but the difference, although statistically significant with $P = 0.007$, was very small and is doubtful to have any significant physiological impact.

The molecular profiles of VLC/ELC CEs in WT corneas closely replicated the profiles of those in meibum (Figs. 10A, 10B). Notably, the overall presence of meibomian-type VLC/ELC CEs in WT mouse cornea samples varied from sample to sample – in some cases, they were undetectable, whereas, in the others, meibomian-type CEs comprised up to 4% of the total CE pool. For these reasons, corneal ELC CEs were tentatively attributed to the remnants of MLs that originated from the TFLL, but not the corneas themselves. This hypothesis was further tested in transcriptomic experiments (see below).

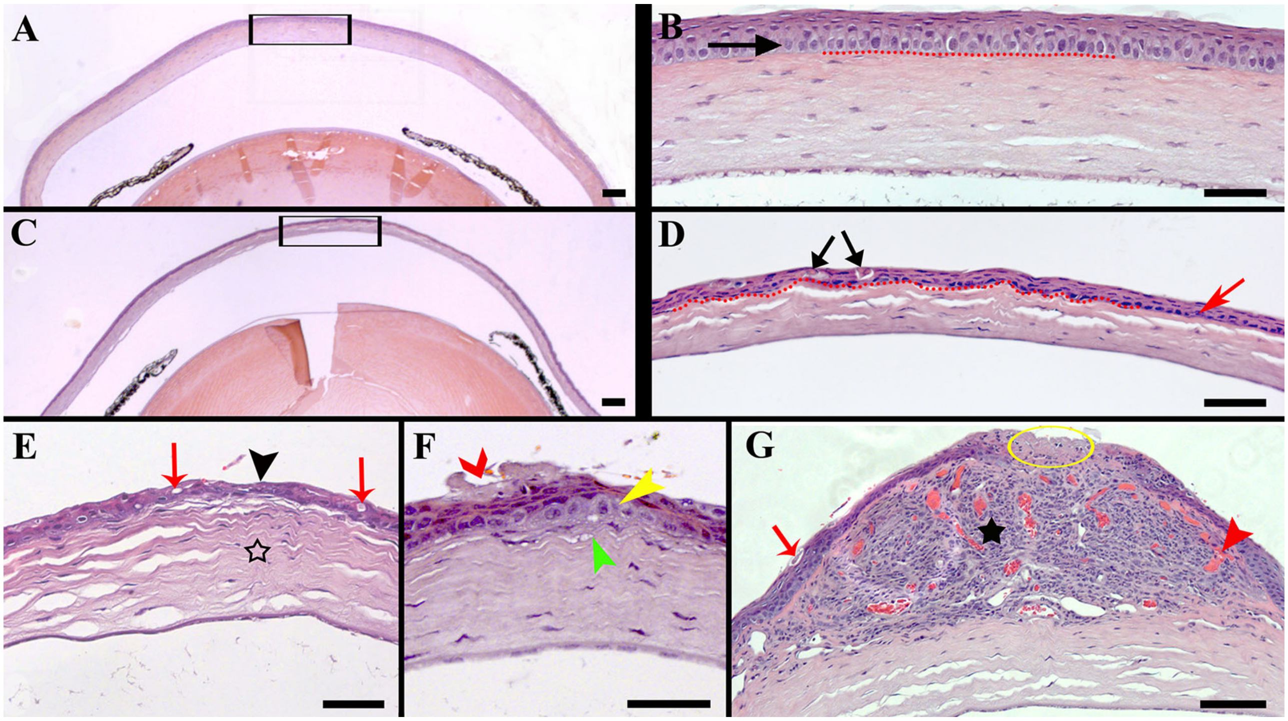

Figure 6. Histopathologic changes to the cornea. (**A**) Three-month-old WT cornea with the typical morphology of the stroma and epithelium. (**B**) WT cornea with a smooth junction between the stroma and epithelium (*red dashed line*) and healthy basal epithelial cells (*black arrow*). (**C**) *Soat1*$^{-/-}$ 3-month-old cornea is noticeably thinner than the WT cornea (*black box*). (**D**) The basal epithelial cells are flat (*red arrow*) with areas of apoptotic cells (*black arrows*) and a jagged interface between the stroma and epithelium (*red dashed line*). (**E**) Eight-month-old *Soat1*$^{-/-}$ cornea with epithelial vacuoles (*red arrows*), focal edema (*star*), and epithelial deterioration (*black arrowhead*). (**F**) Epithelial degeneration (*red chevron*), hydropic change of the basal cell (*yellow arrowhead*), and sub epithelial vacuoles (*green arrowhead*). (**G**) Twelve-month-old ulcerated (*yellow circle*) cornea with neovascularization (*red arrowhead*), fibrosis, and inflammatory cells (*black star*). Hematoxylin and eosin (H&E) staining. Scale bars in panels **A**, **C**, and **G** = 100 µm. Scale bars in panels **B**, **D**, **E**, and **F** = 50 µm.

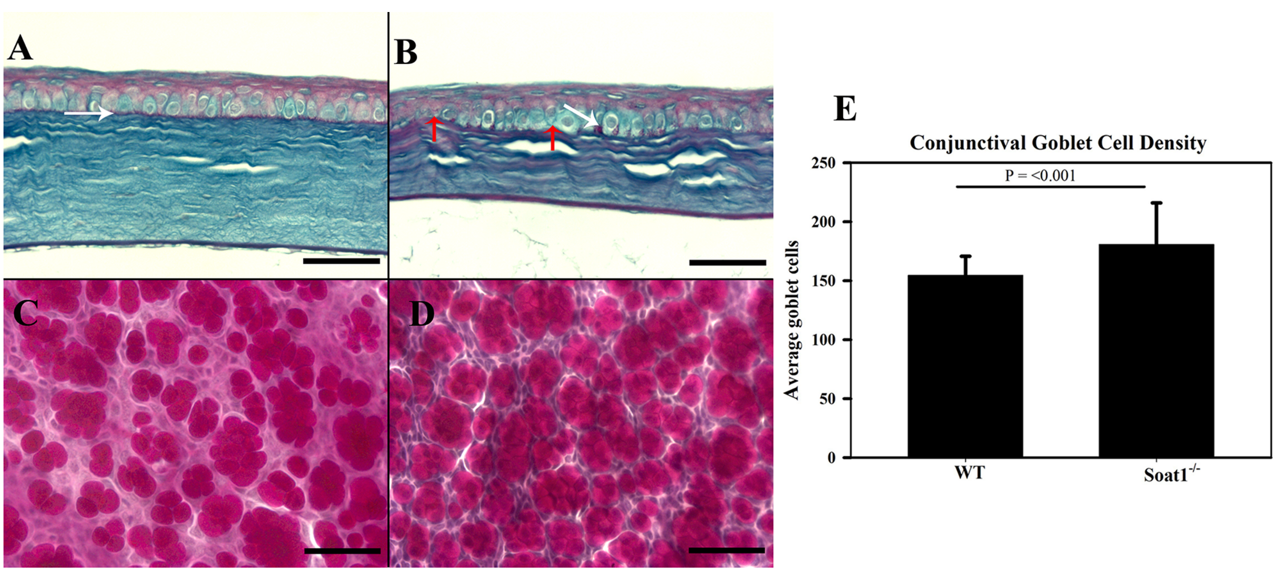

Figure 7. Periodic acid—Schiff staining of the corneal basement membrane and conjunctival goblet cells. (**A**) WT basement membrane was uniform across the entirety of the cornea (*white arrow*) compared to (**B**) the *Soat1*$^{-/-}$ cornea with frequent breaks (*red arrow*) in the BM and areas with accumulations of PAS positive material (*white arrow*). (**C**) WT conjunctival goblet cells stained with PAS. (**D**) *Soat1*$^{-/-}$ conjunctival goblet cells that had increased goblet cells in the conjunctival fornix. (**E**) WT conjunctiva had less goblet cells compared to the goblet cells in the *Soat1*$^{-/-}$ conjunctiva. PAS staining. Scale bars = 50 µm.

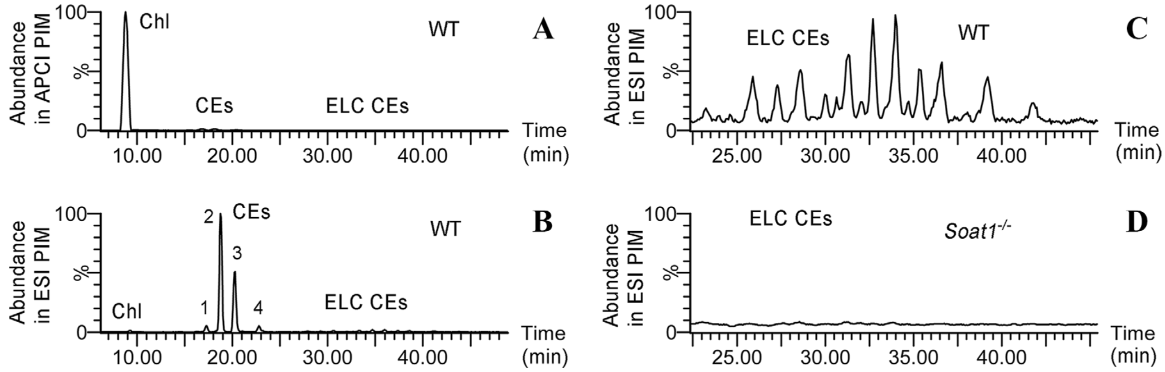

Figure 8. LC-MS analysis of cornea cholesteryl esters (CEs) of wild type (WT) and *Soat*$^{-/-}$ mice. Extracted ion chromatograms of the Chl and CE common analytical ion with *m/z* value of 369.35 are shown. (**A**) Overall CE profile of WT corneas. Non-esterified cholesterol (Chl) is detected as the major species in APCI PIM. (**B**) Normal length plasma-type CEs detected in all WT and *Soat*$^{-/-}$ corneas in ESI PIM: (1) $C_{18:1-}$, (2) $C_{18:2-}$, (3) $C_{20:4-}$, and (4) $C_{22:6}$–CEs. Note that ESI PIM is more sensitive for CEs than free Chl, producing a much smaller peak of Chl. (**C**) The fraction of very and extremely long chain CEs (VLC/ELC CEs) in WT mice is present, but widely varies from sample to sample. (**D**) The fraction VLC/ELC CEs in *Soat*$^{-/-}$ mice is non-existent in all tested *Soat1*$^{-/-}$ corneas.

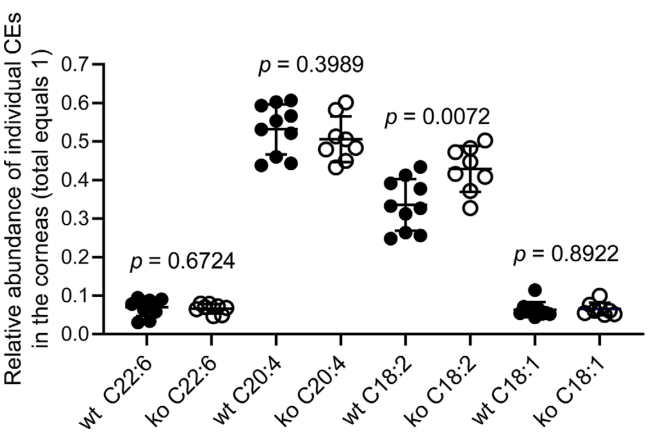

Figure 9. Relative abundance of normal length plasma-type $C_{18:1-}$, $C_{18:2-}$, $C_{20:4-}$, and $C_{22:6}$–CEs in corneas of wild type (wt; $n = 10$) and *Soat*$^{-/-}$ (ko; $n = 8$) mice.

Transcriptomic Analysis of Tarsal Plates and Corneas of Wild Type and *Soat1*$^{-/-}$ Mice

Comparison of Tarsal Plate and Cornea Transcriptomes of Wild-Type Mice. Next, the entire transcriptomes of WT TPs and corneas were compared using scatter and Volcano plots (Figs. 11A, 11B). There were about 66,000 unique transcripts identified, of which approximately 39,000 passed the selection criteria of a $P < 0.05$ and a linear fold change (LFC) of $-2 \geq \text{LFC} \geq 2$. Of these TP transcripts, 4625 were found to be upregulated, while 34,327 were downregulated. Clearly, the transcriptomes of TPs and corneas bared no resemblance to each other and were further evaluated using more selective criteria. To reduce the massive number of transcripts that were to be analyzed, the non-coding, micro-RNA, tRNA, small RNA, ribosomal, and unassigned transcripts were filtered out, resulting in approximately 16,000 known protein-coding, multiple-complex, and pseudogenes, which were included in the subsequent, more focused, analyses.

As a first step, the *Soat1* and *Soat2* expression levels in TPs and cornea were determined (Fig. 11C). It was found that *Soat2* was present in both tissues at identically low levels (around 4.35 ± 0.05 on a log2 scale). In contrast, *Soat1* was highly expressed in TPs (17.6 ± 0.3), but much less in the cornea (7.4 ± 0.2), with a TP-to-cornea LFC of over 1000. Importantly, a related gene – *Lcat/Slc12a4* – that encodes enzyme lecithin-cholesterol acyltransferase (LCAT), was found in mouse TPs and corneas only at a very low log2 level of 4.7 ± 0.1 for both tissues.

In an attempt to connect lipid profiles of TPs and corneas with their transcriptomes, we conducted targeted evaluation of TPs and cornea mRNA profiles focusing on the rest of the main genes of meibogenesis.[19–21] A heatmap of approximately 50 main genes that are involved in meibogenesis and/or differ significantly between TPs and corneas are shown in Figure 11D (data from Supplementary Table S1). The vast differences in the expression levels of these genes between TPs and corneas corroborated the results of our lipidomic experiments as no genes related to the generation of typical VLC/ELC ML (such as WE, CEs, [*O*]-acylated omega-hydroxy FAs [OAHFAs], and CEs of OAHFAs [Chl-OAHFAs] that require *Elovl3*, *Elovl4*, *Far1/Far2*, *Awat1/Awat2*, and others to be synthesized) were found to be expressed at substantial levels, except for a few genes related to cholesterol biosynthesis, such as *Dhcr24*, *Hmgcs1*, *Idi2*, *Fdps*, and *Fdft1*.

Tarsal Plate Transcriptomes of Wild Type and Soat1-Knockout Mice. Previously, *Soat1* inactivation was shown to result in an almost complete arrest of VLC/ELC CE production in *Soat1*$^{-/-}$ MGs, but the glands retained their ability to supply shorter chain serum-like CEs to meibum with only minor changes in their WE or triacylglycerol profiles.[11] These specific effects were accompanied by dramatic changes in the mouse ocular phenotype, which affected not only TPs, but also the mouse cornea and other ocular structures (see Figs. 2–7). Importantly, the *Soat1*-inactivation mutation did not have any effect on the expression levels of a related gene *Soat2* in either tissue, which retained its log2 value (4.4 in WT and 4.3 in *Soat1*$^{-/-}$ mice; $P = 0.9$).

When the mouse TP transcriptomic data was analyzed using the Integrated Molecular Pathway Level Analysis (IMPaLA) version 13.0 web tool (found at http://impala.molgen.mpg.de), specifically its pathway over-

Investigative Ophthalmology & Visual Science

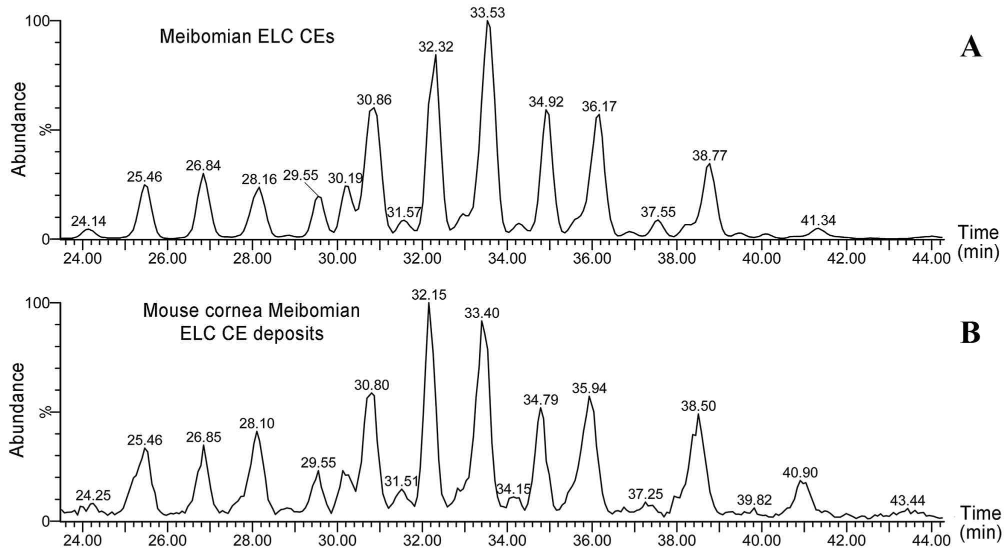

Figure 10. Comparative analysis of very and extremely long chain cholesteryl esters (VLC/ELC CEs) observed in meibomian glands and corneas of wild type mice. Extracted ion chromatograms of an analytical ion *m/z* 369.35 are shown. (**A**) An LC/MS ESI PIM profile of VLC/ELC CEs obtained directly from meibomian glands. (**B**) VLC/ELC CEs detected in the corneas of wild type mice. Representative chromatograms are shown. Note a very close similarities of the CE profiles in both types of samples.

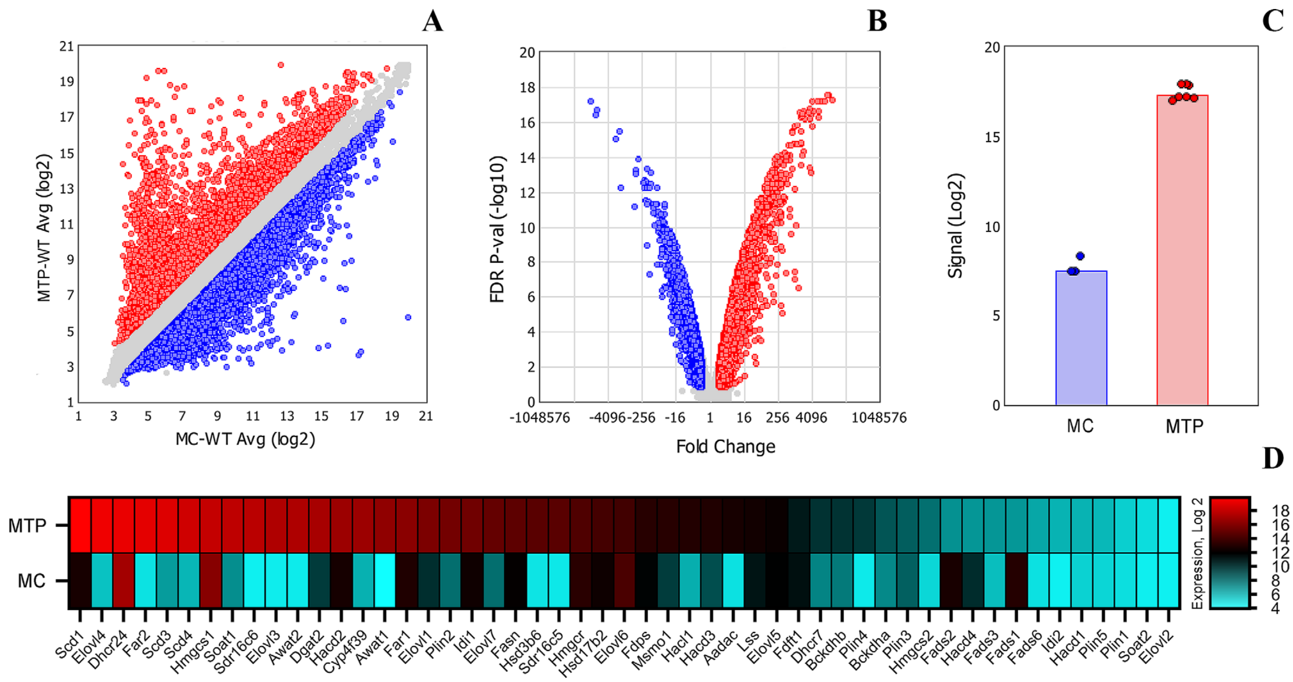

Figure 11. Comparative analysis of mouse tarsal plates (MTP; shown in *red*) and cornea (MC; shown in *blue*) transcriptomes of wild type (WT) mice. (**A**) A scatter plot reveals high dissimilarity between MTP and MC tissues. (**B**) A Volcano plot was used to estimate the statistical significance of fold changes in specific genes between MTP and MC tissues. (**C**) The expression levels of *Soat1* in MC and M are significantly different. (**D**) A heat map of the expression levels of major genes of meibogenesis in MTP and mouse corneas MC.

representation and Wilcoxon pathway enrichment analyses tools, and the PANTHER Knowledge Database (http://pantherdb.org), a number of up- and downregulated pathways with P-genes and Q-genes values below 0.05 were identified (Table and Supplementary Table S2).

Among pathways downregulated with the highest statistical significance, there were pathways responsible for general metabolism, keratinization, FA metabolism, lipid metabolism, cholesterol metabolism, muscle contraction, striated muscle contraction, glucose metabolism, O-linked glycosylation of mucins, among other functions, whereas highly upregulated pathways included RNA metabolism, mitosis, and cell division in general. In addition, notably upregulated genes were responsible for formation, modification, and trimerization of collagen, SUMOylation, extracellular matrix reorganization, and, controversially, de novo FA

Table. Most Up-and Down-Regulated Pathways in Tarsal Plates of *Soat1*-Null Mice.

Pathway Name	Number of Overlapping Genes	Number of All Pathway Genes	P-Genes	Q-Genes
Most downregulated pathways in MGs of Soat1-null mice				
Metabolism (general)	224	1952	7.99E-24	3.74E-20
Keratinization	39	129	9.71E-18	2.27E-14
Metabolism of lipids	97	645	1.79E-17	2.79E-14
Muscle contraction	42	174	4.08E-15	4.77E-12
Striated muscle contraction pathway	19	35	6.34E-14	5.93E-11
Fatty acid metabolism	39	176	7.54E-13	5.88E-10
Striated muscle contraction	16	35	3.56E-11	2.38E-08
Gluconeogenesis	15	34	2.76E-10	1.62E-07
Cardiac muscle contraction - Homo sapiens (human)	23	87	1.02E-09	5.31E-07
Diabetic cardiomyopathy – H. sapiens (human)	36	203	4.13E-09	1.93E-06
Glycolysis and gluconeogenesis	14	45	2.13E-07	8.33E-05
Fatty acid beta-oxidation	12	34	3.35E-07	0.000121
Super-pathway of conversion of glucose to acetyl CoA and entry into the TCA cycle	14	47	3.9E-07	0.000131
Electron transport chain (OXPHOS system in mitochondria)	21	103	6.74E-07	0.00021
Super-pathway of cholesterol biosynthesis	10	25	8.47E-07	0.000224
Glutathione metabolism - Homo sapiens (human)	15	57	8.9E-07	0.000224
Non-alcoholic fatty liver disease - Homo sapiens (human)	26	150	9.32E-07	0.000224
Glutathione conjugation	12	37	9.58E-07	0.000224
O-linked glycosylation of mucins	16	66	1.29E-06	0.000232
Oxidation of branched chain fatty acids	7	12	1.7E-06	0.000232
Most upregulated pathways in MGs of Soat1-null mice				
Metabolism of RNA	108	583	6.17E-14	2.89E-10
Processing of capped intron-containing pre-mRNA	58	241	1.09E-12	2.56E-09
Cell cycle	106	621	2.15E-11	3.36E-08
Mitotic prometaphase	47	192	8.35E-11	9.77E-08
Mitotic anaphase	47	195	1.47E-10	1.16E-07
Resolution of sister chromatid cohesion	33	109	1.49E-10	1.16E-07
Mitotic metaphase and anaphase	47	196	1.78E-10	1.19E-07
M Phase	73	382	2.03E-10	1.19E-07
Cell cycle_ mitotic	90	523	5.01E-10	2.60E-07
mRNA Splicing - major pathway	43	177	6.86E-10	3.09E-07
mRNA Processing	35	127	7.26E-10	3.09E-07
mRNA Splicing	43	185	2.96E-09	1.15E-06
PLK1 Signaling events	18	44	1.14E-08	4.11E-06
Chromatin modifying enzymes	53	271	2.85E-08	8.91E-06
Chromatin organization	53	271	2.85E-08	8.91E-06
SUMOylation	40	182	5.53E-08	1.62E-05
Separation of sister chromatids	32	130	7.43E-08	1.96E-05
SUMO E3 ligases SUMOylate target proteins	39	177	7.53E-08	1.96E-05
EML4 and NUDC in mitotic spindle formation	27	100	1.01E-07	2.48E-05
Amplification of signal from unattached kinetochores via a MAD2 inhibitory signal	26	96	1.62E-07	3.61E-05

and squalene/cholesterol biosynthesis, among other pathways (see Table and Supplementary Table S2). Note that the number of genes for the last two processes were not as large as those that were downregulated, and a heavy reliance on the genes of the NUP family (nucleoporins) in making those conclusions leaves room for alternative explanations.

To determine whether inactivation of *Soat1* had any effect on the lipid homeostasis in MGs, expression levels of major genes of meibogenesis in TPs of WT and $Soat1^{-/-}$ mice were compared (Fig. 12). It appeared that almost all genes of interest underwent either up- or downregulation, but the magnitude of the effects varied widely. Of 360 genes tested, 86 genes were downregulated in the $Soat1^{-/-}$ TPs with a WT-to-$Soat1^{-/-}$ LFC of > (+2), whereas 21 genes were upregulated with LFC < (−2) (Supplementary Table S3). The rest of the changes in these genes were outside of the default LFC criterion of ≤ (−2) or ≥ (+2). Moreover, less than 50% of the genes underwent statistically significant changes with $P \leq 0.05$, with most of them being expressed at relatively low levels. Interestingly, two key genes of WE biosynthesis – *Awat1* and *Awat2* – were significantly downregulated in the MGs of $Soat1^{-/-}$ mice (see Supplementary Table S3).

Cornea Transcriptomes of Wild-Type and *Soat1*-Knockout Mice. Human and mouse cornea transcriptome have been described and discussed earlier.[27–30] Inactivation of *Soat1* in mice caused a noticeable perturbation in the cornea gene expression profiles (GEP; Supplementary Table S4). When the data for *Soat1*-null and WT corneas were compared using the IMPaLA Pathway Analysis Web tool, among the most upregulated pathways with P-gene and Q-gene values of <0.05 in *Soat1*-null mice were those related to: (1) activation of angiogenesis via VEGFA-VEGFR2 signaling pathway[31–33]; (2) glycolysis, gluconeogenesis, Cori cycle, and carbohydrate

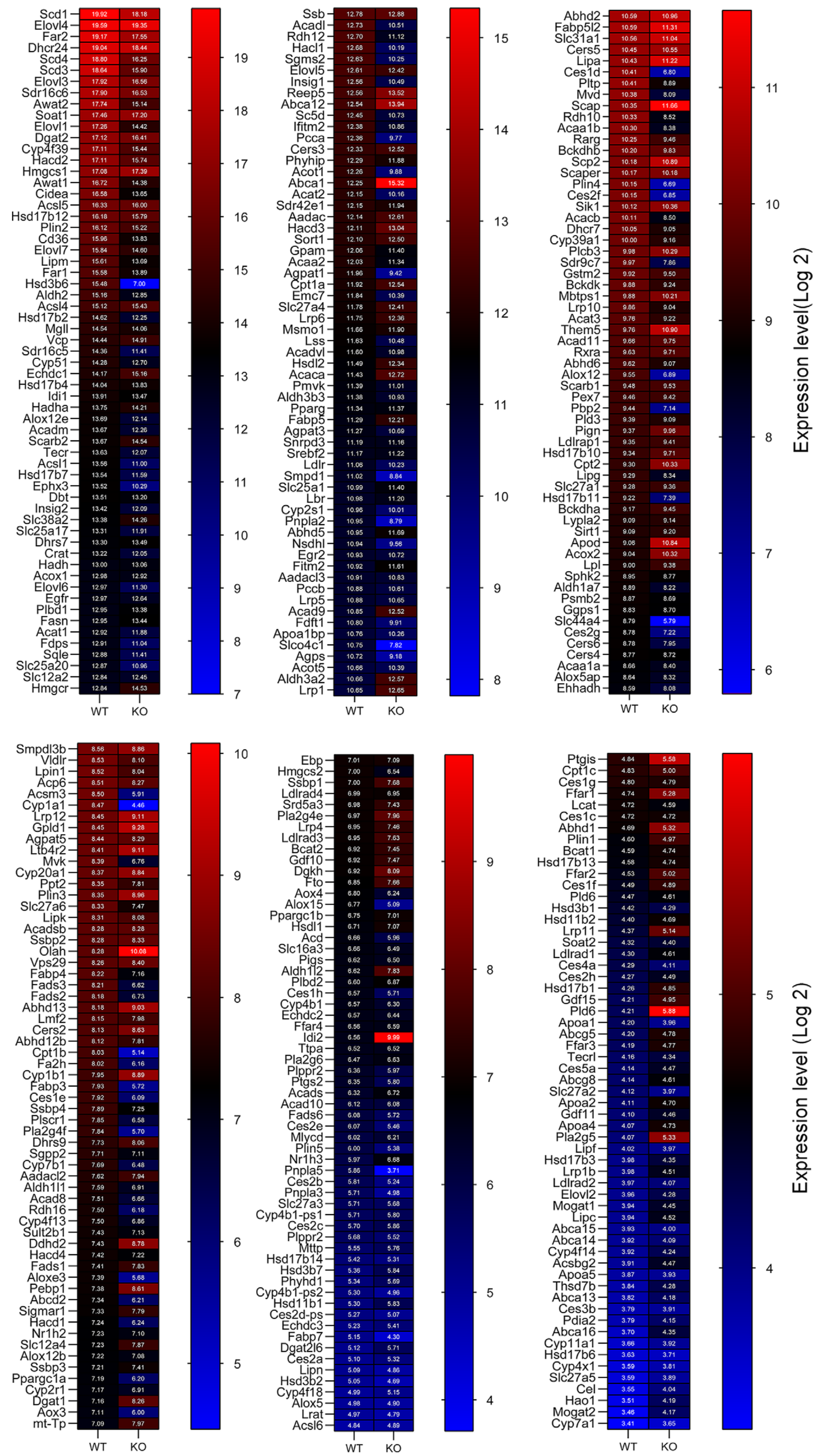

Figure 12. Expression levels of 360 major genes of meibogenesis in tarsal plates of wild type (WT) and *Soat1*$^{-/-}$ (KO) mice.

metabolism in general (https://pubchem.ncbi.nlm.nih.gov/pathway/WikiPathways:WP1946); (3) keratinization, ossification, collagen formation, and extracellular matrix organization; and (4) various cell signaling pathways that are involved in hypoxia, stress, apoptosis, and immune responses, among others (Supplementary Table S5). The number of downregulated pathways with P-gene values of <0.05 was considerably smaller, with none of them producing Q-gene values of <0.05 (Supplementary Table S6). The only downregulated pathway that approached the level of statistical significance of a Q-gene value of 0.07 was the SLC-mediated transmembrane transport pathway, whereas, for the rest of them, the Q-gene values were >0.3. To better understand some of these changes, a more targeted analysis of the GEP in WT and *Soat1*-null corneas was conducted as follows.

Neovascularization/Angiogenesis. An overview of corneal neovascularization in experimental transgenic mouse models can be found in a review by Kather and Kroll.[34] Consistent with neovascularization of the corneas of *Soat1*-null mice observed in our histological experiments (see Fig. 6), VEGFA-VEGFR2 signaling pathway was seemingly activated. Specifically upregulated from log2 (7.61) to log2 (9.36) was *Vegfa* (LFC = 3.36; $P = 2.8 \times 10^{-6}$), with no changes in the expression levels of *Vegfb* and *Vegfc* genes. However, no correlation of the changes in the GEP with an earlier publication of Wang et al.[35] was found, except for downregulation of *Tgm2*, *Sorbs2* (*Sorbs1* in the paper[35]), and *Gsta4* [ibid], and upregulation of *S100a4*/*S100a7a* (*S100a9*/*S100a8* [ibid]). Yet another gene to consider is *Il36a*/*IL36a*, which is a promoter of angiogenesis in humans[36] and an ortholog of the mouse gene *El1f8*.[37] Importantly, the latter was shown to participate in the activation of the Nf-κb pathway (discussed below). Also noticeable was an increase in *Mmp2* (log2 values of 11.39 in WT and 12.38 in mutants; LFC = 2; $P = 0.0002$), which plays multiple roles in various processes, including angiogenesis and inflammation (discussed below).[38,39]

Opacification and Keratinization of Cornea. Although our histological observations did not provide a direct evidence of cornea (hyper)keratinization in young mice, it became visible with aging mice. Transcriptomic data demonstrated clear and significant upregulation of the relevant pathway(s) (see Supplementary Table S5). Among genes that are involved in (hyper)keratinization, there were *Sprr1a* and *Sprr1b* genes which encode small proline-rich proteins SPRR1A and SPRR1B.[40] These genes were highly upregulated in the corneas of *Soat1*-null mice: the WT-to-mutant LFC of *Sprr1a* and *Sprr1b* genes were 198 ($P = 4.5 \times 10^{-6}$) and 170 ($P = 1.9 \times 10^{-10}$), correspondingly (see Supplementary Table S4). Other genes of the keratinization pathway, such as *Krt17*, *Ivl*, *Krt19*, *Tgm1*, *Cds*, *Krt10*, *Krt14*, and *Spink5*, were also notably upregulated (ibid).

Hypoxia, Apoptosis, and Inflammation. The *Plk3*/*c-Jun* signaling pathway is known to be involved in hypoxic stress and apoptosis in the cornea. In particular, activation of polo-like kinase 3 *Plk3*/PLK3 induces c-JUN phosphorylation in the central part of the cornea but not in the limbal region.[41] We observed upregulation of at least 3 genes of this pathway – *Plk3*, *Jun*, and *Hif1a* – in *Soat1*-null corneas. The log2 expression level of *Plk3* was increased from 5.69 in WT corneas to 8.54 in the mutant ones (LFC = 7.2; $P = 2.5 \times 10^{-8}$). Other members of the *Plk* family (*Plk1*, *Plk2*, *Plk4*, and *Plk5*) were also increased, but to a much lower extent with log2 values of 1.07 to 1.64. The *Jun* levels were also highly upregulated from log2 8.52 in WT mice to 12.46 in the mutants (LFC = 15.3; $P = 6.2 \times 10^{-8}$). Finally, *Hif1a* was also increased from 13.3 to 13.9 (LFC = 1.5; $P = 2 \times 10^{-4}$).

Another cluster of relevant genes are *MMPs* that encode matrix metallopeptidases, which are implicated in various processes, including apoptosis and inflammation.[42,43] In our experiments, only 4 *MMP* genes out of 19 detected were found to be noticeably increased in *Soat1*$^{-/-}$ corneas with *P* values approaching, or exceeding, the statistically significant levels of $P = 0.05$: *Mmp2* (log2 values of 11.39 in WT and 12.38 in mutants; LFC = 2; $P = 0.0002$), *Mmp3* (5.26 in WT and 7.36 in mutants; LFC = 4.3; $P = 0.06$), *Mmp13* (4.8 in WT and 5.76 in mutants; LFC = approximately 2; $P = 0.05$), and *Mmp19* (5.76 in WT and 6.45 in mutants; LFC = 1.6; $P = 8 \times 10^{-5}$). All four genes have been clearly linked to inflammatory processes in various tissues. Interestingly, *Mmp9* – a reportedly potent player in cornea neovascularization, inflammation and ulceration[44,45] – was not changed in the *Soat1*$^{-/-}$ corneas (4.4 in WT mice and 4.5 in the mutant mice, respectively; LFC = −1.03).

An important marker of inflammation to consider was *Nlrp3*,[44] a member of a large *Nlr* family of genes. Contrary to Shimizu et al.,[44] neither its levels, nor levels of other *Nlrp* genes, were changed in the *Soat1* mutant mice remaining at very low *log*2 values of 4 to 5 regardless of the genotype. Similarly unaffected by the mutation were *Il18* and functionally related genes *Il18bp*, *Il18r*, and *Il18rap*.[46] Interleukin 18 (IL-18) is a potent cytokine that, among other functions, regulates innate and acquired immune response,[47,48] and is considered a suitable diagnostic marker for various disorders. However, its expression levels remained steady at log2 values of 8.2 with no fold changes ($P < 0.3$). Conversely, *Il1f8*[49] – an ortholog of a human *IL36b* gene (see Reference 37 and https://www.ncbi.nlm.nih.gov/gene/69677) – demonstrated a 4.5-fold increase ($P = 0.1$) in response to the *Soat1* inactivating mutation, and so did the *Nfkbia* gene that encodes a transcription factor NF-κB[50] (also a part of inflammasome regulation), which was increased from 9.62 to 11.26 with an LFC of 3.1 ($P = 4 \times 10^{-7}$).

Discussion

Effects of Soat1 Inactivation on Meibomian Glands and Meibum

Inactivation of *Soat1* – one of the major genes of meibogenesis that is highly expressed in TPs of mice and humans (for both species, 17.5 ± 0.5 on a log2 scale) – was previously shown to dramatically reduce biosynthesis of VLC/ELC CEs in MGs of mice, while preserving some amounts of shorter chain CEs and leading to the accumulation of nonesterified Chl in their TPs.[21] At the same time, the expression levels of *Soat1* and *Soat2* in the WT corneas, reported in this study, were rather low with log2 values of approximately 7.4 and approximately 4.4, correspondingly (see Fig. 11), and so were the expression levels of *Lcat* (log2 = approximately 4.6). The levels of the final lipid products of meibogenesis in mouse MGs positively correlated with the levels of expression of corresponding metabolically related genes. For example, the levels of *Soat1* and CEs correlated in a quasi-linear fashion, and so did the levels of WE and *Awat2* and *Elovl3* genes. Importantly, it was not until the *Soat1* expression level exceeded 10 on a log2 scale that VLC/ELC CEs started to accumulate in MGs in large quantities.[21] Also noteworthy are the extremely low corneal expression levels of *Elovl3* (log2 of 4.5) and *Elovl4* (log2 of 5.9; see Fig. 11, Supplementary Table S1), which are essential for the biosynthesis of VLC/ELC FA – essential precursors for meibomian-type lipids, including VLC/ELC CEs,[10,16] and which are absent from the cornea lipidome. Therefore, it seems possible to predict an impact of a gene that encodes a major metabolically important enzyme on the basis of its expression level in a given tissue and conclude that VLC/ELC CEs that were randomly observed in WT mice were not the products of in situ biosynthesis in the mouse cornea.

Characteristically, the VLC/ELC CEs profiles in WT and *Soat1*$^{-/-}$ corneas were almost identical (see Fig. 10). This fact, in combination with lack of expression of essential genes of meibogenesis in corneas (see Fig. 11), signifies that VLC/ELC CEs in the WT cornea specimens originated, in fact, from the MGs, and were uncontrollably deposited on the corneas as remnants of the TF lipids. Furthermore, LC-MS analysis of shorter chain CEs in WT and *Soat1*$^{-/-}$ corneas revealed only negligible differences in their profiles (see Fig. 9). Some other organs and tissues, for example, the liver, colon, cerebral cortex, and cerebrospinal fluid, plasma, and serum, and others, express and/or contain considerable amounts of LCAT (GeneCards, https://www.genecards.org/cgi-bin/carddisp.pl?gene=LCAT), which can then circulate with blood across the body.[51,52] Together with LCAT, SOAT2 (https://www.genecards.org/cgi-bin/carddisp.pl?gene=SOAT2) produces shorter-chain, plasma-like CEs,[53] and, therefore, both enzymes can be considered to be legitimate sources of regular CEs for the cornea. Thus, the shorter chain CEs, such as $C_{18:1-}$, $C_{18:2-}$, $C_{20:4-}$, and $C_{22:6}$–CEs, could have been biosynthesized either in situ (i.e. within MGs) by SOAT2 and/or LCAT, or produced in distant loci and transported to the corneas with the blood stream.

There could be numerous pathophysiological consequences of the *Soat1* inactivation. Two of the most obvious outcomes is solidification of abnormal meibum at physiological temperatures[11] and dramatic changes in the rheological properties of ML once they are augmented with nonesterified Chl.[54] A sharp increase in the melting temperature of *Soat1*$^{-/-}$ meibum is mostly due to the accumulation of nonesterified Chl (which melts at approximately 145–150°C), at the expense of CEs with much lower melting temperatures.[55] Moreover, in our previous study,[54] we tested the effects of free Chl on rheological properties of human meibum using the Langmuir trough and determined that incremental increases in the Chl-to-total ML ratio led to progressive stiffening of the lipid films and increased their collapsibility once the Chl-to-meibum ratio exceeded 5% (w/w). In homozygous *Soat1*-null mice, nonesterified Chl becomes the most prominent lipid dominating the entire lipid pool. In addition, solidification of meibum has a detrimental impact on meibum expressibility from the orifices and cause dilation of central ducts and MG orifices. Taken together, these factors are likely to be responsible for lessening the protective properties of meibum on the ocular surface and may cause stagnation of abnormal lipid in the ductules of MGs of *Soat1*$^{-/-}$ mice.

Thus, it was reasonable to conclude that the major, if not all, effects of *Soat1* inactivation on the cornea and MGs homeostasis could have arisen from the effects of meibomian-type VLC/ELC CEs ablation and accumulation of free, nonesterified Chl in meibum.

The vast changes in the ocular phenotype of *Soat1*$^{-/-}$ mice homozygous for the *Soat1* mutation included severe anatomic abnormalities in their eyelids and corneas. One of the most visible features of the eyes of knockout mice was their abnormal shape – a slit-eye phenotype with the ellipticity of 0.92 ± 0.01, which clearly differentiated *Soat1*$^{-/-}$ mice from their WT counterparts with virtually round eyes. This abnormal mouse phenotype has been found to be a characteristic outcome of inactivating mutations in other genes involved in meibogenesis, for example, *Elovl3*,[10,56] *Elovl4*,[16] *Awat2*,[13,14] *Sdr16c5/Sdr16c6*,[12,57] *Far1/Far2*,[58,59] and *Cyp4f39*.[18] Considering that these mutations result in abnormal meibum with deficiencies in clearly different groups of lipids, it was surprising to come to a conclusion that any tested major alteration in meibomian lipidome causes similar reshaping and minimization of the palpebral fissure of mutant mice regardless of their genotypes. It is not clear whether these changes are voluntary (or spontaneous) happening in an attempt to minimize the ocular surface irritation, or if they were caused by a slew of detrimental structural changes in the eyelids and adnexa. Our analysis of the TP transcriptome of *Soat1*-knockout mice revealed strong evidence of downregulation of the Muscle Contraction and Striated Muscle Contraction Pathways, compared to their WT littermates. Specifically, genes *Tnni2*, *Myom1*, *Tnnt3*, *Ttn*, *Des*, *Tcap*, *Actn2*, *Tnnc2*, *Myl1*, *Actn3*, *Acta1*, *Mybpc1*, *Mybpc2*, and *Neb*, among others, were affected. As striated Riolan's muscles that are found in MGs are believed to help and/or regulate meibum secretion,[60] downregulation of these pathways will likely impede the muscle contraction and relaxation cycle, and, hence, dysregulate meibum delivery onto the ocular surface. Simultaneously, the striated orbicularis oculi and levator palpebrae superioris muscles that control eye blinking and squeezing may also be affected by the mutation, which could play a significant role in the congenital and/or acquired dysmorphism of the palpebral fissures of the *Soat1*-knockout mice.

Effects of Soat1 Inactivation on Mouse Cornea

For the reader's convenience, a diagram that summarizes the effects of *Soat1* inactivation on ocular surface homeostasis in mice is shown in Figure 13. The 10 most highly upregulated genes in *Soat1*$^{-/-}$ corneas were *Sprr1a* and *Sprr1b* followed by *Ptgs2*, *Jun*, *Dusp1*, *Cdsn*, *Kprp*, *Spink5*, *Gm5941*, and *S100a7a* (see Supplementary Table S4). Until now, there was only limited information on their functions in the cornea, which prompted us to briefly summarize some of their known activities in the cornea and other tissues. However, due to the high magnitude of their dysregulation in mutant corneas, we expect these genes and proteins to be evaluated in future studies in more detail.

Sprr1a and *Sprr1b*. Small proline-rich proteins SPRR1A and SPRR1B, called cornifins, are encoded by genes *Sprr1a* and *Sprr1b*. These keratinocyte proteins participate in the formation of cell envelopes in cornifying stratified epithelia,[61] one of whose functions is to increase mechanical resistance of tissues to deformation stress. In addition, an increase in SPRR1A was reported in mouse corneas that were subjected to desiccating stress.[62] Indicatively, the *Jun* gene was also upregulated in *Soat1*-null corneas, similarly to its increase in desiccating stress conditions studied by de Paiva et al. [ibid]. Coincidentally, *Sprr1b* was found to be a valid biomarker for squamous metaplasia in human subjects with Sjogren's syndrome and mouse models of dry eye,[63] whereas *Sprr1a* is considered to be a regeneration-associated protein.

Interestingly, Newsome et al.[64] described an open eyelids with cleft palate (*oel*) mouse with hyperkeratinized ocular surface that exhibited poor wetting characteristics, thickened and vacuolated BM, and progressive opacification of the cornea. To the best of our knowledge, this mutation is currently not linked to any specific chromosome or gene, but the phenotype of *oel* mice partially resembles the ocular features of *Soat1*$^{-/-}$ mice.

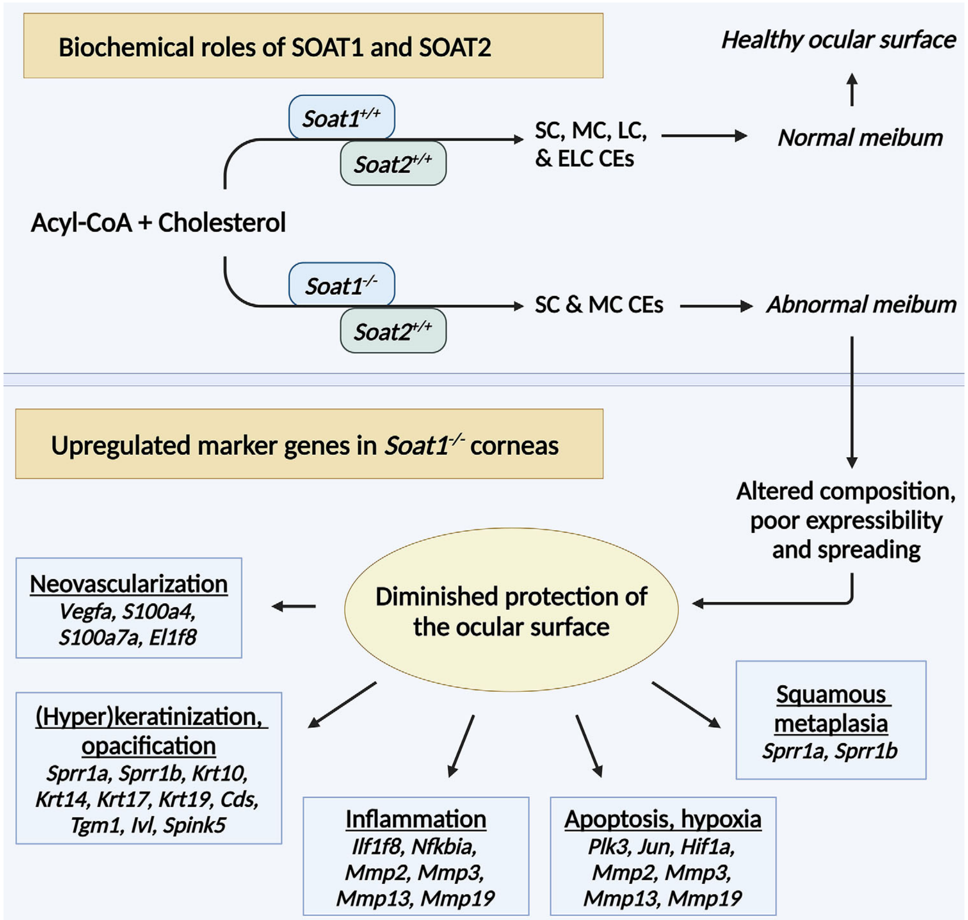

Figure 13. The effects of *Soat1* inactivation on the mouse ocular surface homeostasis. SC – short chain, MC – medium length chain, LC – long chain, ELC – extremely long chain, CEs – cholesteryl esters.

Cdsn. Corneodesmosin (CDSN) – a secreted glycoprotein that plays an important role in cohesion of cells, such as corneocytes,[65] – is encoded by the gene *Cdsn*. Its known functions are related almost exclusively to human epidermis and other cornified squamous epithelia (https://ncbi.nlm.nih.gov/gene/1041). In our experiments, its expression in mouse corneas went up considerably in response to *Soat1* inactivation from relatively low log2 values of 6.9 to 10.1 ($P < 0.08$; see Supplementary Table S4).

Ptgs2 and Vegfa. Another frequent abnormality in *Soat1*$^{-/-}$ mice was neovascularization of their corneas (see Figs. 2B, 6G). Our transcriptomic data implies that PTGS2 and VEGFA-VEGFR2 signaling pathways are significantly upregulated in *Soat1*$^{-/-}$ corneas (see Supplementary Tables S4, S5). The *Ptgs2* gene encodes inducible cyclooxygenase-2 (COX2)[66] which is a key enzyme in the biosynthesis of prostaglandins (PGs). One of its products, specifically PGE2, is an important signaling molecule for activation of the VEGF signaling pathway.[67,68] At the same time, *Ptgs2/*COX2, unlike its constitutive counterpart COX1, participates in wound healing of the cornea and is upregulated in stromal keratocytes.[66]

S100a4. The S100 calcium-binding protein A4 (S100A4) is involved in inflammatory processes and thought to have pro-angiogenic activity in tumor development and inflamed cornea.[69] These functions may be related to the development of the *Soat1*$^{-/-}$ phenotype in mice and correlate well with our observation of cornea neovascularization in the mutants.

Jun. Our results demonstrated that the expression levels of *Jun* in mouse cornea was highly increased in *Soat1*-null mice with LFC of >15 (see Supplementary Table S4). The c-JUN N-Terminal kinases (JNKs) are the most important mitogen-activated protein kinases (MAPKs) which have crucial roles in several cellular processes, such as apoptosis, autophagy, and inflammation.[70,71] The c-JUN, a member of activator protein-1 (AP-1), is the main substrate of JNKs. The c-JUN has been thought to participate in two fundamental mechanisms: apoptosis and autophagy acting via the JNK signaling pathway. Activated JNKs in mitochondrial matrix migrate to nucleus and phosphorylate c-JUN and other transcription factors. The c-JUN/AP-1 dependent activation results in and increase in the transcription of pro-apoptotic genes which trigger apoptosis. Phosphorylation of c-Jun also mediates the transcription of autophagic genes.[71] The other important signaling pathway, Polo-like kinase 3 (Plk3), causes the corneal epithelial cell death in response to hypoxic stress and hyperosmotic stress conditions (see Reference 72 and https://doi.org/10.1074/jbc.M116.725747). It has been shown that the increased Plk3 kinase activity has a direct effect on the phosphorylation of c-JUN corneal epithelial cells [ibid].

Dusp1. Dual specificity phosphatase 1 (DUSP1) is a mediator in the resolution of inflammation[73] and has a protective anti-inflammatory role in osteoarthritis. It also participates in cellular responses to environmental stress (https://ncbi.nlm.nih.gov/1843). In cultured keratoconic corneal stromal cells, its expression level is five times of that in the norm.[74]

S100a7a. Another S100 calcium binding protein A7A (S100A7A) was demonstrated to have antimicrobial activity against *Staphylococcus aureus* and *Haemophilus influenze*, but not *E. coli*, and suggested to be a component of the ocular surface innate immune system.[75]

Kprp. Keratinocyte proline rich protein KPRP participates in keratinocyte differentiation and was reported to be expressed in human skin (https://ncbi.nlm.nih.gov/448834). In mice, KPRP plays a role in the epidermal barrier function[76] as *Kprp*-knockout mice demonstrated an increase in transepidermal loss of water.

Spink5. The functions of serine peptidase inhibitor Kazal type 5 (SPINK5) in the cornea are also largely unknown. In a recent publication,[77] Kim et al. suggested a role for SPINK5, in conjunction with its effector, STAT3, in maintaining skin barrier homeostasis. Loss of SPINK5 function due to a mutation results in a genetic disease called Netherton syndrome,[78,79] whose characteristic signs are an impaired skin barrier (which was linked to lipid abnormalities), allergic reactions, inflammation, and stratum corneum detachment.[80]

Il1f8. The of IL1F8/IL36B is a key part of a IL-36 signaling pathway (see References 37, 49, and 81 and https://www.ncbi.nlm.nih.gov/gene/27177) which activates NF-κB[37] and is related to neutrophilic inflammation and angiogenesis.[36]

Finally, the predicted gene *Gm5941* has no known functions at this time.

Conclusions

Summarizing our observations and data published by other laboratories, one can suggest a direct involvement of *Soat1/*SOAT1 of meibomian glands, and extremely long chain cholesteryl esters they produce, in maintaining ocular surface homeostasis, in general, and the health of the cornea, specifically. It is also reasonable to assume that a sharp accumulation of free, nonesterified cholesterol in *Soat1*$^{-/-}$ meibum is responsible not only for its abnormally poor expressibility and spreadability due to the high melting temperature of the secretion, but can also trigger, promote and/or mediate inflammation in the eye and adnexa similarly to the mechanisms related to the onset of atherosclerosis and obesity.[82] It is also likely that upregulation of marker genes of apoptosis, inflammation, neovascularization, keratinization, and muscle contraction in the meibomian glands and/or cornea are downstream effects of *Soat1* inactivation, similar to those in *Elovl3*- null mice,[10,56] despite being caused by depletion of entirely different types of meibomian lipids.

Acknowledgments

The authors would like to express their gratitude to Matthew Petroll and the Core grant P30 EY030413 for providing access to the Zeiss fluorescent microscope that was used for taking images of stained tissue sections. Figure 13 was created using BioRender.

Funded by the U.S. National Institutes of Health R01 grant EY027349 (to I.A.B.).

Disclosure: **A. Wilkerson**, None; **S. Yuksel**, None; **R. Acharya**, None; **I.A. Butovich**, None

References

1. McCann P, Abraham AG, Mukhopadhyay A, et al. Prevalence and incidence of dry eye and meibomian gland dysfunction in the United States: a systematic review and meta-analysis. *JAMA Ophthalmol.* 2022;140(12):1181–1192.
2. Akowuah PK, Kobia-Acquah E, Donkor R, et al. Prevalence of meibomian gland dysfunction in Africa: a systematic review and meta-analysis of observational studies. *Ophthalmic Epidemiol.* 2022;29:374–383.
3. Bikbov MM, Kazakbaeva GM, Rakhimova EM, et al. The prevalence of dry eye in a very old population. *Acta Ophthalmol.* 2022;100:262–268.
4. Bikbov MM, Gilmanshin TR, Zainullin RM, et al. Prevalence and associations of dry eye disease and meibomian gland dysfunction in the ural eye and medical study. *Sci Rep.* 2022;12:18849.
5. Chan AYY, Chuang JC, Wong VWY. Evaluation of meibomian gland dysfunction among ophthalmic healthcare workers. *Clin Ophthalmol.* 2021;15:1201–1206.
6. Amano S, Inoue K. Estimation of prevalence of meibomian gland dysfunction in Japan. *Cornea.* 2017;36:684–688.
7. Rathnakumar K, Ramachandran K, Baba D, et al. Prevalence of dry eye disease and its association with dyslipidemia. *J Basic Clin Physiol Pharmacol.* 2018;29:195–199.
8. Chatterjee S, Agrawal D, Sharma A. Meibomian gland dysfunction in a hospital-based population in central India. *Cornea.* 2020;39:634–639.
9. Donthineni PR, Kammari P, Shanbhag SS, Singh V, Das AV, Basu S. Incidence, demographics, types and risk factors of dry eye disease in India: electronic medical records driven big data analytics report I. *Ocul Surf.* 2019;17:250–256.
10. Butovich IA, Wilkerson A, Bhat N, McMahon A, Yuksel S. On the pivotal role of Elovl3/ELOVL3 in meibogenesis and ocular physiology of mice. *FASEB J.* 2019;33:10034–10048.
11. Butovich IA, Wilkerson A, Yuksel S. Depletion of cholesteryl esters causes meibomian gland dysfunction-like symptoms in a Soat1-null mouse model. *Int J Mol Sci.* 2021;22(4):1583.
12. Butovich IA, Wilkerson A, Goggans KR, Belyaeva OV, Kedishvili NY, Yuksel S. Sdr16c5 and Sdr16c6 control a dormant pathway at a bifurcation point between meibogenesis and sebogenesis. *J Biol Chem.* 2023;299:104725.
13. McMahon A, Yuksel S, Bhat N, Pham H, Wilkerson A, Butovich IA. Inactivation of Awat2 in mice causes loss of wax ester lipids from meibum. *Invest Ophthalmol Vis Sci.* 2020;61:2632.
14. Widjaja-Adhi MAK, Silvaroli JA, Chelstowska S, et al. Deficiency in Acyl-CoA:wax alcohol acyltransferase 2 causes evaporative dry eye disease by abolishing biosynthesis of wax esters. *FASEB J.* 2020;34(10):13792–13808.
15. Sassa T, Tadaki M, Kiyonari H, Kihara A. Very long-chain tear film lipids produced by fatty acid elongase ELOVL1 prevent dry eye disease in mice. *FASEB J.* 2018;32:2966–2978.
16. McMahon A, Lu H, Butovich IA. A role for ELOVL4 in the mouse meibomian gland and sebocyte cell biology. *Invest Ophthalmol Vis Sci.* 2014;55:2832–2840.
17. Agbaga MP. Different mutations in ELOVL4 affect very long chain fatty acid biosynthesis to cause variable neurological disorders in humans. *Adv Exp Med Biol.* 2016;854:129–135.

18. Miyamoto M, Sassa T, Sawai M, Kihara A. Lipid polarity gradient formed by omega-hydroxy lipids in tear film prevents dry eye disease. *Elife*. 2020;9:e53582.
19. Butovich IA, McMahon A, Wojtowicz JC, Lin F, Mancini R, Itani K. Dissecting lipid metabolism in meibomian glands of humans and mice: an integrative study reveals a network of metabolic reactions not duplicated in other tissues. *Biochim Biophys Acta*. 2016;1861:538–553.
20. Butovich IA. Meibomian glands, meibum, and meibogenesis. *Exp Eye Res*. 2017;163:2–16.
21. Butovich IA, Wilkerson A. Dynamic changes in the gene expression patterns and lipid profiles in the developing and maturing meibomian glands. *Int J Mol Sci*. 2022;23(14): 7884.
22. Lemp MA. Report of the National Eye Institute/Industry workshop on Clinical Trials in Dry Eyes. *CLAO J*. 1995;21: 221–232.
23. Butovich IA, Wilkerson A, Yuksel S. Dysregulation of lipid metabolism in aging meibomian glands and its molecular markers. *Int J Mol Sci*. 2023;24(17):13512.
24. McCann LC, Tomlinson A, Pearce EI, Diaper C. Tear and meibomian gland function in blepharitis and normals. *Eye Contact Lens*. 2009;35:203–208.
25. McCulley JP, Dougherty JM, Deneau DG. Classification of chronic blepharitis. *Ophthalmology*. 1982;89:1173–1180.
26. Driver PJ, Lemp MA. Meibomian gland dysfunction. *Surv Ophthalmol*. 1996;40:343–367.
27. Gottsch JD, Seitzman GD, Margulies EH, et al. Gene expression in donor corneal endothelium. *Arch Ophthalmol*. 2003;121:252–258.
28. Kinoshita S, Adachi W, Sotozono C, et al. Characteristics of the human ocular surface epithelium. *Prog Retin Eye Res*. 2001;20:639–673.
29. Jiao X, Wu M, Lu D, Gu J, Li Z. Transcriptional profiling of daily patterns of mRNA expression in the C57BL/6J mouse cornea. *Curr Eye Res*. 2019;44:1054–1066.
30. Tasheva ES, Ke A, Deng Y, et al. Differentially expressed genes in the lens of mimecan-null mice. *Mol Vis*. 2004;10:403–416.
31. Phillips GD, Stone AM, Jones BD, Schultz JC, Whitehead RA, Knighton DR. Vascular endothelial growth factor (rhVEGF165) stimulates direct angiogenesis in the rabbit cornea. *In Vivo*. 1994;8:961–965.
32. Kenyon BM, Voest EE, Chen CC, Flynn E, Folkman J, D'Amato RJ. A model of angiogenesis in the mouse cornea. *Invest Ophthalmol Vis Sci*. 1996;37:1625–1632.
33. Dan Cosnita AR, Raica M, Sava MP, Cimpean AM. Gene expression profile of vascular endothelial growth factors (VEGFs) and platelet-derived growth factors (PDGFs) in the normal cornea. *In Vivo*. 2021;35:805–813.
34. Kather JN, Kroll J. Transgenic mouse models of corneal neovascularization: new perspectives for angiogenesis research. *Invest Ophthalmol Vis Sci*. 2014;55:7637–7651.
35. Wang W, Deng M, Li M, Liu L, Zou J, Qian Y. Exploring corneal neovascularization: an integrated approach using transcriptomics and proteomics in an alkali burn mouse model. *Invest Ophthalmol Vis Sci*. 2024;65:21.
36. Komaki R, Miyagaki T, Tanaka M, et al. Increased interleukin-36beta expression promotes angiogenesis in Japanese atopic dermatitis. *Int J Mol Sci*. 2023;24(13):11104.
37. Towne JE, Garka KE, Renshaw BR, Virca GD, Sims JE. Interleukin (IL)-1F6, IL-1F8, and IL-1F9 signal through IL-1Rrp2 and IL-1RAcP to activate the pathway leading to NF-kappaB and MAPKs. *J Biol Chem*. 2004;279:13677–13688.
38. Quintero-Fabian S, Arreola R, Becerril-Villanueva E, et al. Role of matrix metalloproteinases in angiogenesis and cancer. *Front Oncol*. 2019;9:1370.
39. Manicone AM, McGuire JK. Matrix metalloproteinases as modulators of inflammation. *Semin Cell Dev Biol*. 2008;19:34–41.
40. Koizumi H, Kartasova T, Tanaka H, Ohkawara A, Kuroki T. Differentiation-associated localization of small proline-rich protein in normal and diseased human skin. *Br J Dermatol*. 1996;134:686–692.
41. Wang L, Gonzalez S, Dai W, Deng S, Lu L. Effect of hypoxia-regulated polo-like kinase 3 (Plk3) on human limbal stem cell differentiation. *J Biol Chem*. 2016;291:16519–16529.
42. Xie Y, Mustafa A, Yerzhan A, et al. Nuclear matrix metalloproteinases: functions resemble the evolution from the intracellular to the extracellular compartment. *Cell Death Discov*. 2017;3:17036.
43. Lee HS, Kim WJ. The role of matrix metalloproteinase in inflammation with a focus on infectious diseases. *Int J Mol Sci*. 2022;23(18):10546.
44. Shimizu H, Sakimoto T, Yamagami S. Pro-inflammatory role of NLRP3 inflammasome in experimental sterile corneal inflammation. *Sci Rep*. 2019;9:9596.
45. Goncalves FM, Jacob-Ferreira AL, Gomes VA, et al. Increased circulating levels of matrix metalloproteinase (MMP)-8, MMP-9, and pro-inflammatory markers in patients with metabolic syndrome. *Clin Chim Acta*. 2009;403:173–177.
46. Rex DAB, Agarwal N, Prasad TSK, Kandasamy RK, Subbannayya Y, Pinto SM. A comprehensive pathway map of IL-18-mediated signalling. *J Cell Commun Signal*. 2020;14:257–266.
47. Wawrocki S, Druszczynska M, Kowalewicz-Kulbat M, Rudnicka W. Interleukin 18 (IL-18) as a target for immune intervention. *Acta Biochim Pol*. 2016;63:59–63.
48. Ihim SA, Abubakar SD, Zian Z, et al. Interleukin-18 cytokine in immunity, inflammation, and autoimmunity: biological role in induction, regulation, and treatment. *Front Immunol*. 2022;13:919973.
49. Barksby HE, Lea SR, Preshaw PM, Taylor JJ. The expanding family of interleukin-1 cytokines and their role in destructive inflammatory disorders. *Clin Exp Immunol*. 2007;149:217–225.
50. Liu T, Zhang L, Joo D, Sun SC. NF-κB signaling in inflammation. *Signal Transduct Target Ther*. 2017;2:17023.
51. Flores R, Jin X, Chang J, et al. LCAT, ApoD, and ApoA1 expression and review of cholesterol deposition in the cornea. *Biomolecules*. 2019;9(12):785.
52. Murata Y, Maeda E, Yoshino G, Kasuga M. Cloning of rabbit LCAT cDNA: increase in LCAT mRNA abundance in the liver of cholesterol-fed rabbits. *J Lipid Res*. 1996;37:1616–1622.
53. Zhang J, Sawyer JK, Marshall SM, et al. Cholesterol esters (CE) derived from hepatic sterol O-acyltransferase 2 (SOAT2) are associated with more atherosclerosis than CE from intestinal SOAT2. *Circ Res*. 2014;115:826–833.
54. Arciniega JC, Uchiyama E, Butovich IA. Disruption and destabilization of meibomian lipid films caused by increasing amounts of ceramides and cholesterol. *Invest Ophthalmol Vis Sci*. 2013;54:1352–1360.
55. Ginsburg GS, Atkinson D, Small DM. Physical properties of cholesteryl esters. *Prog Lipid Res*. 1984;23:135–167.
56. Wilkerson A, Bhat N, Quoc Hai Pham H, Yuksel S, Butovich I. Physiological effects of inactivation and the roles of Elovl3/ELOVL3 in maintaining ocular homeostasis. *FASEB J*. 2021;35:e21327.
57. Wu L, Belyaeva OV, Adams MK, et al. Mice lacking the epidermal retinol dehydrogenases SDR16C5 and SDR16C6 display accelerated hair growth and enlarged meibomian glands. *J Biol Chem*. 2019;294:17060–17074.

58. Cheng JB, Russell DW. Mammalian wax biosynthesis. I. Identification of two fatty acyl-coenzyme A reductases with different substrate specificities and tissue distributions. *J Biol Chem.* 2004;279:37789–37797.
59. Otsuka K, Sawai-Ogawa M, Kihara A. Formation of fatty alcohols-components of meibum lipids-by the fatty acyl-CoA reductase FAR2 is essential for dry eye prevention. *FASEB J.* 2022;36:e22216.
60. Knop E, Knop N, Millar T, Obata H, Sullivan DA. The international workshop on meibomian gland dysfunction: report of the subcommittee on anatomy, physiology, and pathophysiology of the meibomian gland. *Invest Ophthalmol Vis Sci.* 2011;52:1938–1978.
61. Hohl D, de Viragh PA, Amiguet-Barras F, Gibbs S, Backendorf C, Huber M. The small proline-rich proteins constitute a multigene family of differentially regulated cornified cell envelope precursor proteins. *J Invest Dermatol.* 1995;104:902–909.
62. De Paiva CS, Pangelinan SB, Chang E, et al. Essential role for c-Jun N-terminal kinase 2 in corneal epithelial response to desiccating stress. *Arch Ophthalmol.* 2009;127:1625–1631.
63. Li S, Nikulina K, DeVoss J, et al. Small proline-rich protein 1B (SPRR1B) is a biomarker for squamous metaplasia in dry eye disease. *Invest Ophthalmol Vis Sci.* 2008;49:34–41.
64. Newsome DA, Harne LC, Brown KS, Hassell JR. Corneal keratinization in the oel/+ mouse. *Curr Eye Res.* 1982;2:553–560.
65. Jonca N, Guerrin M, Hadjiolova K, et al. Corneodesmosin, a component of epidermal corneocyte desmosomes, displays homophilic adhesive properties. *J Biol Chem.* 2002;277:5024–5029.
66. Amico C, Yakimov M, Catania MV, Giuffrida R, Pistone M, Enea V. Differential expression of cyclooxygenase-1 and cyclooxygenase-2 in the cornea during wound healing. *Tissue Cell.* 2004;36:1–12.
67. Kamal MV, Damerla RR, Dikhit PS, Kumar NA. Prostaglandin-endoperoxide synthase 2 (PTGS2) gene expression and its association with genes regulating the VEGF signaling pathway in head and neck squamous cell carcinoma. *J Oral Biol Craniofac Res.* 2023;13:567–574.
68. Kamal MV, Damerla RR, Parida P, et al. Expression of PTGS2 along with genes regulating VEGF signalling pathway and association with high-risk factors in locally advanced oral squamous cell carcinoma. *Cancer Med.* 2024;13:e6986.
69. Li C, Zhang F, Wang Y. S100A proteins in the pathogenesis of experimental corneal neovascularization. *Mol Vis.* 2010;16:2225–2235.
70. Dhanasekaran DN, Reddy EP. JNK signaling in apoptosis. *Oncogene.* 2008;27:6245–6251.
71. Chen J, Ye C, Wan C, et al. The roles of c-Jun N-terminal kinase (JNK) in infectious diseases. *Int J Mol Sci.* 2021;22(17):9640.
72. Wang L, Dai W, Lu L. Hyperosmotic stress-induced corneal epithelial cell death through activation of Polo-like kinase 3 and c-Jun. *Invest Ophthalmol Vis Sci.* 2011;52:3200–3206.
73. Hoppstadter J, Ammit AJ. Role of dual-specificity phosphatase 1 in glucocorticoid-driven anti-inflammatory responses. *Front Immunol.* 2019;10:1446.
74. Saee-Rad S, Raoofian R, Mahbod M, et al. Analysis of superoxide dismutase 1, dual-specificity phosphatase 1, and transforming growth factor, beta 1 genes expression in keratoconic and non-keratoconic corneas. *Mol Vis.* 2013;19:2501–2507.
75. Garreis F, Gottschalt M, Schlorf T, et al. Expression and regulation of antimicrobial peptide psoriasin (S100A7) at the ocular surface and in the lacrimal apparatus. *Invest Ophthalmol Vis Sci.* 2011;52:4914–4922.
76. Suga H, Oka T, Sugaya M, et al. Keratinocyte proline-rich protein deficiency in atopic dermatitis leads to barrier disruption. *J Invest Dermatol.* 2019;139:1867–1875.e1867.
77. Kim J, Kim MG, Jeong SH, Kim HJ, Son SW. STAT3 maintains skin barrier integrity by modulating SPINK5 and KLK5 expression in keratinocytes. *Exp Dermatol.* 2022;31:223–232.
78. Furio L, Hovnanian A. Netherton syndrome: defective kallikrein inhibition in the skin leads to skin inflammation and allergy. *Biol Chem.* 2014;395:945–958.
79. Chavanas S, Bodemer C, Rochat A, et al. Mutations in SPINK5, encoding a serine protease inhibitor, cause Netherton syndrome. *Nat Genet.* 2000;25:141–142.
80. van Smeden J, Janssens M, Boiten WA, et al. Intercellular skin barrier lipid composition and organization in Netherton syndrome patients. *J Invest Dermatol.* 2014;134:1238–1245.
81. Queen D, Ediriweera C, Liu L. Function and regulation of IL-36 signaling in inflammatory diseases and cancer development. *Front Cell Dev Biol.* 2019;7:317.
82. Tall AR, Yvan-Charvet L. Cholesterol, inflammation and innate immunity. *Nat Rev Immunol.* 2015;15:104–116.